

The effect of carbonate assimilation and nanoheterogeneities on the viscosity of phonotephritic melt from Vesuvius

Gabriele Giuliani^{a,*}, Danilo Di Genova^b, Fabrizio Di Fiore^c, Pedro Valdivia^d, Silvio Mollo^{c,e}, Claudia Romano^a, Tiziana Boffa Ballaran^d, Alexander Kurnosov^d, Alessandro Vona^a

^a Dipartimento di Scienze, University of Roma Tre, L.go San Leonardo Murialdo 1, 00146 Roma, Italy

^b Institute of Science, Technology and Sustainability for Ceramics (ISSMC), National Research Council of Italy (CNR), Italy

^c National Institute of Geophysics and Volcanology, Section of Roma 1, Via di Vigna Murata 605, 00143 Roma, Italy

^d Bayerisches Geoinstitut, University of Bayreuth, Universitätsstraße 30, 95440 Bayreuth, Germany

^e Department of Earth Sciences, Sapienza – University of Rome, P. le Aldo Moro 5, 00185 Roma, Italy

ARTICLE INFO

Editor: Don Porcelli

Keywords:

Viscosity measurements
Phonotephritic melt
Carbonate assimilation
Endoskarn formation

ABSTRACT

Interaction between magma and carbonate plays a pivotal role in volcanic systems, yet its impact on magma transport properties remains inadequately explored. This study presents novel viscosity data on a leucite-bearing phonotephritic melt from the 472 CE Pollena eruption (Vesuvius, Italy), doped with varying amounts of CaO and CaO + MgO. The compositions match the chemistry of melt inclusions and interstitial glasses from skarns at Vesuvius, which have been interpreted as related to mixing of magma with different amounts of CaO and MgO derived from the host carbonates (limestone and dolostone). Viscosity measurements were conducted at both high (1150–1400 °C) and low temperatures (640–760 °C) by concentric cylinder viscometry, differential scanning calorimetry, and micropenetration methods. Through an integrated approach which combines Brillouin and Raman spectroscopy with the aforementioned techniques, we accurately predict the viscosity changes induced by magma-carbonate interaction and identify the formation of nanoheterogeneities during low-temperature viscosity measurements. Notably, viscosity models from the literature fail to accurately reproduce our experimental data set at both high and low temperature. In the high-temperature regime, the addition of CaO induces a remarkable viscosity decrease, surpassing that produced by CaO + MgO addition. Furthermore, our findings reveal a significant viscosity/temperature crossover resulting from the addition of CaO and CaO + MgO to the melt phase. Undoped melt exhibits a higher viscosity compared to doped melts above 750 °C, with an inverse trend observed below this temperature threshold. Such rheological constraints may affect the mobility and mixing capability of melts exposed to different levels of carbonate assimilation.

1. Introduction

The interaction between magma and the surrounding country rock may produce melts with compositions significantly distinct from those resulting from simple crystal fractionation within the sub-volcanic plumbing system (Daly, 1910; Hildreth and Moor bath, 1988; Rogers et al., 1985; Sklyarov et al., 2021). Extensively documented in geological records across various volcanoes, the assimilation of calcite- and/or dolomite-bearing carbonate rocks by magma gives rise to the formation of stratified shells, categorized as “exoskarns” and “endoskarns” (Deegan et al., 2010; Del Moro et al., 2001; Di Stefano et al., 2018; Foland et al., 1993; Kerrick, 1977; Lentz, 1999; Wenzel et al., 2002).

Exoskarns originate from thermal metamorphic reactions induced in the host protolite by magmatic-hydrothermal fluids, diffusion of chemical constituents from the adjacent magmatic intrusion, or a combination of both processes. Endoskarns correspond to the crystallization of desilicated CaO- and/or CaO-MgO-rich melts during substantial carbonate assimilation by magma. The heating of carbonate wall-rocks produces calcium-rich melts that readily mix with the silicate magma to form a hybrid melt, which may directly crystallize melilite due to silica depletion (Conte et al., 2009; Lustrino et al., 2022). Alternatively, melilite may form via equilibration at sub-solidus conditions in the exoskarn shells (Wenzel et al., 2002; Whitley et al., 2020). It has been also documented that the amount of CO₂ released during

* Corresponding author.

E-mail address: gabriele.giuliani@uniroma3.it (G. Giuliani).

<https://doi.org/10.1016/j.chemgeo.2024.122408>

Received 20 May 2024; Received in revised form 9 September 2024; Accepted 10 September 2024

Available online 12 September 2024

0009-2541/© 2024 The Authors. Published by Elsevier B.V. This is an open access article under the CC BY license (<http://creativecommons.org/licenses/by/4.0/>).

magma-carbonate interaction at subduction zones is minimally produced from the magma itself (<11 %) and is instead predominantly generated from the decarbonation of wall-rocks within the metamorphic aureole surrounding the magma body (>89 %) (Morris and Canil, 2024).

The interaction between magma and carbonate induces the diffusion of Ca^{2+} and Mg^{2+} into the melt phase with consequent changes in the physicochemical properties of the magma, such as density and viscosity (Colucci et al., 2024; Knuever et al., 2023a,b). Despite the obvious implications of this process for magma dynamics, there is no literature exploring from an experimental standpoint the influence of varying degrees of carbonate contamination on melt viscosity. With the aim of addressing this issue, here we present measurements on the high- and low-temperature viscosity of melts, mimicking the assimilation of variable amounts of calcite and dolomite by the phonotephritic magma from the 472 CE Pollena subplinian eruption (Vesuvius, Italy). The eruptive products from the Pollena eruption include xenoliths of different types of exoskarns and endoskarns, interpreted as the outcome of variable degrees of decarbonation reactions in a relatively shallow magma chambers (8–10 km) within a thick calcite- and dolomite-bearing carbonate crust (Bruno et al., 1998; Cioni et al., 1998; Del Moro et al., 2001; Fulignati et al., 2004; Iacono Marziano et al., 2007a,b, 2008; Iacono Marziano et al., 2007b; Jolis et al., 2013, 2015; Sulpizio et al., 2005, 2007; Vona et al., 2020).

The rheological effect of the increasing amount of CaO and $\text{CaO} + \text{MgO}$ contents in the melt was characterized through concentric cylinder viscometry at high-temperature, and micropenetration and differential scanning calorimetry techniques at low-temperature. In addition, differential scanning calorimetry, Brillouin, and Raman spectroscopy were collectively employed to quantitatively constrain the effect of Fe-Ti-oxide nanocrystallization during viscosity measurements and its role in hindering the derivation of crystal-free viscosity (Di Genova et al., 2017a,b, 2020; Kleest and Webb, 2022; Liebske et al., 2003; Okumura et al., 2022; Scarani et al., 2022a; Valdivia et al., 2023, 2024).

Results show that the addition of CaO alone affects more extensively the melt viscosity compared to the addition of CaO and MgO . Intriguingly, chemically-based literature models (Giordano et al., 2008; Langhammer et al., 2022) fail to predict the viscosity of magma-carbonate interaction experiments, whilst the Brillouin spectroscopy-based model (Cassetta et al., 2021) yields superior performance. Finally, we explore the rheological control of carbonate assimilation during endoskarn formation, hybrid magma mixing, and transport dynamics at Vesuvius.

2. Methods

2.1. Starting materials

The starting material is a leucite-bearing phonotephrite from the 472 CE Pollena eruption whose rheological behaviour has been experimentally investigated by Di Fiore et al. (2023, 2021).

Following the same procedure described in Mollo and Vona (2014), approximately 500 g of the phonotephrite sample was reduced to a homogeneous powder in a ball mill and grounded to pass through a #200 mesh sieve. Afterwards, the rock powder was doped with CaO produced by thermal decomposition of variable amounts of CaCO_3 (i.e., $\text{CaCO}_3 \text{ solid} \rightarrow \text{CaO solid} + \text{CO}_2 \text{ gas}$), as CaO is an unstable compound at atmospheric pressure conditions. In detail, a first aliquot of powder was doped with only ~8 or ~17 wt% CaO (i.e., ~14 or ~30 wt% CaCO_3), whereas a second aliquot of powder was doped with ~4 or ~11 wt% CaO (i.e., ~7 or ~20 wt% CaCO_3) plus addition of ~5 wt% or ~15 wt% MgO . Both undoped and doped rock powders were melted in a previously Fe-saturated Pt crucible using a Nabertherm® furnace at 1400 °C and air redox conditions. The melt was held at constant temperature for approximately 5 h and then quenched to glass in air. Based on Raman spectroscopy and SEM imaging, no microlite and nanolite crystals were detected in the synthesized glasses (Di Genova et al., 2017b; Kleest et al., 2020). Finally, Archimedean buoyancy was performed to measure

densities of glasses, with an associated error of $\pm 0.05 \text{ g/cm}^3$.

2.2. Microprobe analysis

Major element compositions of experimental glasses were determined by an electron probe micro-analyser (EPMA) JEOL JXA-8200 equipped with five wavelength dispersive spectrometers (WDS) and installed at the Bayerisches Geoinstitut (University of Bayreuth, Germany). Analyses were performed on carbon-coated thin sections under high vacuum conditions, using an accelerating voltage of 15 kV and an electron beam current of 5 nA, with a defocused beam diameter of 10 μm . Elemental counting times were 20 s on the peak and 5 s on each of the two background positions. Corrections for interelement effects were made using a ZAF (Z: atomic number; A: absorption; F: fluorescence) procedure. Synthetic wollastonite (Ca, Si), periclase (Mg), hematite (Fe), spinel (Al), orthoclase (K), albite (Na), manganese titanite (Mn, Ti) and apatite (P) were used as a calibration standard. Sodium and potassium were analysed first to prevent alkali migration effects. BCR-2 was used as a quality monitor standard and for the calculation of accuracy and precision. Based on counting statistics, accuracy was better than 1–5 %, except for elements with abundances below 1 wt%, for which accuracy was better than 5–10 %. Precision was typically better than 1–5 % for all analysed elements.

2.3. Concentric cylinder viscosity measurements

Viscosity measurements at high temperature were conducted using the concentric cylinder (CC) viscometer at the Experimental Volcanology and Petrology laboratory (EVPLab, University of Roma Tre, Italy) following the methodology outlined by Dingwell (1986). The viscometer head featured a torque full-scale of 75 mNm. Prior to high-temperature (HT) experiments, glass chips from distinct melting batches underwent remelting in a $\text{Pt}_{80}\text{Rh}_{20}$ crucible. The molten samples were stirred at 10 s^{-1} using a $\text{Pt}_{80}\text{Rh}_{20}$ spindle under air redox conditions at 1400 °C for 3 h to ensure chemical and thermal homogeneity (Di Fiore et al., 2022, 2024). The rheometer was calibrated against the NIST 717a standard reference material, ensuring an accuracy of 0.06 log units (Di Fiore et al., 2022). Temperature measurements employed a S-type thermocouple with an accuracy of ± 2 °C. The initial temperature measurement was set at 1400 °C, aligning with a *superliquidus* state of the melt, while a shear rate ($\dot{\gamma}$) of 10 s^{-1} was consistently applied throughout the experiment. Subsequent temperature decrease was carried out incrementally in steps of 50 °C and then 25 °C. At each temperature step, conditions were maintained until a steady torque and temperature were attained (approximately 30–45 min), ensuring precision in the measurement of liquid viscosity (η_{liquid}).

2.4. Micropenetration viscometry measurements

Viscosity measurements at low temperature were performed using a thermomechanical analyser (TMA) and the micropenetration (MP) technique in the range of 693 to 719 °C. The TMA was calibrated against the standard glass DGG-1 (Meerlender, 1974) with a deviation of ± 0.1 in log units. We followed previous protocols (Di Genova et al., 2020; Scarani et al., 2022b; Valdivia et al., 2023) to attain thermal equilibrium and melt relaxation before the viscosity measurement. The measurements were conducted under Ar atmosphere at 1 bar, employing doubly polished glass with a thickness of 3 mm. After thermal equilibration and melt relaxation (10 min), the applied force was 1.47 N (150 g load) for 1 h. The force was decreased to 0.09 N (10 g load) when measuring viscosity below $\sim 10^{9.5} \text{ Pa s}$. Temperature was controlled with an S-type thermocouple (Pt-PtRh) placed at ~ 2 mm from the sample surface. Temperature error, considering the accuracy of the S-type thermocouple and its distance from the sample, was ± 5 °C. The evolution of the indentation depth was monitored over time, and the viscosity curve was determined based on the equation of Douglas et al. (1965). Indentations

ranged between ~ 15 (sample C10M4 at 678°C) and 289 (sample C26M5 at 760°C) microns.

2.5. Differential scanning calorimetry (DSC)

2.5.1. DSC measurements

A DSC 404F3 Pegasus was employed to measure the onset (T_{onset}) and peak temperature (T_{peak}) of heat flow curves over the glass transition temperature interval. Different heating and cooling cycles ($q_{c,h}$) were set at 5, 10 or 20°C min⁻¹ under a constant N₂ flux (5.0 atm at a flow rate of 30 ml min⁻¹) using Pt₈₀Rh₂₀ crucibles. The mass of the glass samples was approximately 25 ± 5 mg. The calibration of the DSC temperature was performed up to $\sim 1050^\circ\text{C}$ using the melting points of reference materials (In, Sn, Bi, Zn, Al, Ag, and Au) (Di Genova et al., 2020; Scarani et al., 2023; Stabile et al., 2021). Baseline measurements were conducted with two empty Pt crucibles. Following the protocol described by Di Genova et al. (2020), each sample was subjected to heating at 10°C min⁻¹ from room temperature to 50°C and maintained at this temperature for 20 min to achieve DSC signal equilibrium. Subsequently, to erase the thermal history of the glass, the temperature was increased with a heating rate of 10°C min⁻¹ to approximately the T_{peak} and then decreased to 50°C at 5, 10 or 20°C min⁻¹. Finally, a matching cycles of $q_{c,h}$ at 5, 10 or 20°C min⁻¹ was applied to derive the T_{onset} and T_{peak} for each $q_{c,h}$.

2.5.2. Literature review of the DSC approach

To derive melt viscosity, shift-factors $K_{onset} = 11.20 \pm 0.15$ and $K_{peak} = 9.84 \pm 0.20$ (Al-Mukadam et al., 2020; Di Genova et al., 2020; Scherer, 1984; Yue et al., 2004) were used in Eq. (1).

$$\log_{10}\eta(T_{peak,onset}) = K_{peak,onset} - \log_{10}(|q_{c,h}|) \quad (1)$$

This approach has been extensively validated and optimized in prior studies (Di Genova et al., 2020, 2023; Scarani et al., 2023; Stabile et al., 2021; Valdivia et al., 2023; Yue et al., 2004) and enables the derivation of viscosity at DSC characteristic temperatures around and slightly above the glass transition temperature (T_g) [$\eta(T_g) = 10^{12}$ Pa s]. Also, the methodology minimizes the risk of chemical and textural alterations, such as (nano)crystallization, thus ensuring the determination of (nano) crystal-free viscosity (Di Genova et al., 2020; Stabile et al., 2021).

Eq. (1) has prompted numerous studies to explore its validity and the consistency of $K_{onset} = 11.3$ across various technical and natural systems. Scherer (1984) demonstrated its use with an alkali lime silicate glass, and subsequent research has shown that this K_{onset} value is applicable across a wide range of compositions. For example, Yue et al. (2004) reported a K_{onset} of 11.35 ± 0.1 for basaltic glass, while Chevrel et al. (2013) found a K_{onset} of 11.2 ± 0.11 for iron-free anorthite–diopside eutectic compositions, averaging 11.04 ± 0.37 for iron-bearing systems. Al-Mukadam et al. (2020) observed $K_{onset} = 11.19 \pm 0.06$ across a range of glass-forming silicate and fluorophosphate systems using high-rate calorimetry. Di Genova et al. (2020) found $K_{onset} = 11.20 \pm 0.15$ when testing a natural basaltic melt from Mt. Etna (Italy) across five compositions, including both fully polymerized and depolymerized silicate systems.

Inspired by extensive literature on the DSC approach for naturally occurring melts (Gottsmann et al., 2002; Potuzak et al., 2008; Stevenson et al., 1995; Webb and Dingwell, 1990; Wilding et al., 1995), it was also determined a second characteristic temperature, corresponding to the heat flow undershoot (T_{peak}) that can be associated with $\eta(T_{peak})$ in Eq. (1).

Our literature review above suggests that K_{onset} is generally independent of melt composition. However, K_{peak} appears to depend on glass composition, especially in silica-rich volcanic systems like rhyolites, as suggested by Stevenson et al. (1995) and Gottsmann et al. (2002). Gottsmann et al. (2002) reported a relationship between K_{peak} and the excess oxides parameter (E.O.), calculated by subtracting the mol% sum

of network formers (excluding SiO₂) from the sum of network modifiers. They found that K_{peak} increased from 9.64 ± 0.08 to 10.80 ± 0.16 with a decreasing E.O. parameter across seventeen iron-bearing glasses, ranging from rhyolites to basalts and basanites. Di Genova et al. (2020) found K_{peak} values between 9.62 and 10.11 for depolymerized standard soda-lime silica glass (DGG-1, Meerlender, 1974) and fully polymerized lithium aluminosilicate glass, respectively, concluding no significant composition dependence of K_{peak} and provided an average of 9.84 ± 0.2 .

Finally, Stabile et al. (2021) calculated K_{onset} and K_{peak} using data from Giordano et al. (2008), which included hydrous iron-free melts in the anorthite–diopside system as a function of $q_{c,h}$ (5, 10, 15, 20, 25 K/min). They found that both K_{onset} and K_{peak} are independent of chemical composition, with values of 11.20 ± 0.03 and 9.78 ± 0.02 , respectively. These findings align with the majority of observations reviewed in this section and their theoretical background (Al-Mukadam et al., 2020; Chevrel et al., 2013; Di Genova et al., 2020; Mazurin, 1977; Moynihan et al., 1976; Potuzak et al., 2008; Scherer, 1984; Webb and Dingwell, 1990). Additionally, Stabile et al. (2021) confirmed that these shift factors are also valid for iron-rich rhyolites with varying alkali content and iron oxidation states.

Here, in this discussion, we test whether the assumption of chemically independent K_{peak} holds also for our melts, and we explore the potential impact of (nano)heterogeneities on the determination of the viscosity of these melts.

2.6. Raman spectroscopy

Samples were structurally characterized both before and after the DSC and micropenetration measurements to test for potential chemical and structural alterations due to temperature exposure above T_g . Analyses were conducted using a Jobin Yvon LABRAM HR800 Horiba equipped with a 532 nm green laser (60 mW nominal power), calibrated with a silicon standard at the EVPLab. Spectra were collected using a 100× objective, covering the range between 100 and 1500 cm⁻¹, with a 30 s acquisition time and 6 accumulations. All spectra were smoothed, baseline subtracted and normalized to the maximum intensity using the code provided in Di Genova et al. (2017b).

2.7. Brillouin spectroscopy

Brillouin spectroscopy measurements (BLS) on glass samples were conducted at the Bayerisches Geoinstitut, Bayreuth, Germany. A solid-state Nd:YVO₄ laser source, emitting at a wavelength of 532 nm and with a power of 50 mW, was employed for the analysis of plane-parallel polished glass samples, each approximately 50 μm thick. Using a six-pass Fabry-Perot interferometer and a single-pixel photon counter detector, the Brillouin frequency shift was measured with a symmetric forward scattering geometry. Calibration of the scattering angle was accomplished using a silica reference glass. Eq. (2) was used to convert frequency shifts ($\Delta\omega$) into longitudinal (V_p) and shear (V_s) sound velocities (Sinogeikin et al., 2006; Whitney and Evans, 2010):

$$\nu = \frac{\Delta\omega\lambda}{2\sin(\theta/2)} \quad (2)$$

where λ represents the laser wavelength and θ is the angle between the incident and scattered beams (i.e., scattering angle of approximately 79.8°). Eight spectra were acquired for each sample at different rotation angles (ranging from -135° to $+180^\circ$) to account for uncertainties. The elastic moduli ratio (K/G) was calculated using the longitudinal (V_p) and shear (V_s) acoustic velocities, as reported in Eq. (3):

$$\frac{K}{G} = \left(\frac{V_p}{V_s}\right) - \frac{4}{3} \quad (3)$$

The melt fragility (m) was calculated after Cassetta et al. (2021):

$$m = 43 \frac{K}{G} - 31 \quad (4)$$

3. Results

3.1. Glass chemistry and K_{peak} calculations

The undoped chemistry of C10M4 is reported in Table 1, showing as primarily compositional features ~51 wt% SiO₂, ~10 wt% CaO and ~4 wt% MgO. For the doped counterpart, C18M5 and C26M5 are enriched in CaO (up to ~26 wt%) and depleted in SiO₂ (down to ~41 wt%) and Na₂O + K₂O (down to ~7 wt%). Similarly, C13M8 and C19M17 are less enriched in CaO (up to ~19 wt%) due to addition of MgO (up to ~17 wt%) and depleted in SiO₂ (down to ~39 wt%) and Na₂O + K₂O (down to ~6 wt%).

According to the TAS classification diagram (total alkali vs. silica; Fig. 1a), the glass composition changes from phonotephrite (C10M4) to tephrite (C18M5) and foidite (C26M5), as the amount of CaO increases. Similarly, the addition of CaO and MgO leads to the formation of phonotephritic (C13M8) and foiditic (C19M17) glasses. It is worth mentioning that the glass compositional range matches the chemistry of melt inclusions and interstitial glasses from magmatic skarns at the Mt. Somma-Vesuvius complex (Del Moro et al., 2001; Fulignati et al., 2000, 2004; Jolis et al., 2015; Fig. 1).

As the concentration of network modifiers cations (Ca²⁺ and Mg²⁺) increases during carbonate assimilation, the melt polymerization is expected to decrease. We use the parameter NBO/T (Mysen et al., 1985) to quantify the number of non-bridging oxygens (NBO) per atom of a tetrahedrally coordinated cation (T). The magnitude of NBO/T increases from 0.42 (C10M4) to 0.74 (C18M5) to 1.14 (C26M5) with CaO addition or, alternatively, it increases to 0.74 (C13M8) and 1.55 (C19M17) upon addition of CaO and MgO (Fig.S5).

3.2. High-temperature viscosity

Viscosities measured at high-temperature using the concentric cylinder apparatus are listed in Table 2 and shown in Fig. 2. Measurements were conducted within the temperature range between 1400 °C and 1150 °C, encompassing a viscosity interval from 10^{0.36} to 10^{2.71} Pa s. For each composition, the lowest temperature is represented by the onset of crystallization. For the sample C26M5, we acknowledge only one data as valid as the stress measured at higher temperatures was considered too low to be converted in viscosity data (i.e., low signal to noise ratio). Fig. 2 shows that at 1250 °C the undoped sample C10M4 has the highest viscosity (10^{2.21} Pa s) compared to doped samples. At the same temperature, an increase in CaO content from ~18 to ~26 wt% leads to a nearly 5-fold decrease in viscosity for C18M5 (10^{1.54} Pa s) and a remarkable 33-fold decrease for C26M5 (10^{0.69} Pa s). In contrast, an

increase in CaO and MgO content from ~21 to ~36 wt% results in a modest decrease in the viscosity for both C13M8 and C19M17 samples, with a 4-fold decrease (10^{1.63} Pa s) for the former and 5-fold decrease (10^{1.54} Pa s) for the latter.

3.3. DSC data

T_{onset} and T_{peak} increase for all samples with increasing cooling/heating rate ($q_{c,h}$). The undoped sample C10M4 has the lowest T_{onset} and T_{peak} for a given cooling/heating rate ($q_{c,h} = 5, 10$ or 20 °C min⁻¹), whilst sample C26M5 with the highest CaO content of 26 wt% displays the highest T_{onset} and T_{peak} at a given $q_{c,h}$. The remaining samples C18M5 (18 wt% CaO), C19M17 (36 wt% CaO + MgO) and C13M8 (21 wt% CaO + MgO) fall in between these two end-members.

The melt viscosity was calculated using Eq. (1) at T_{onset} and T_{peak} of DSC measurements (see data in Table 3), returning values that range from 10^{10.32} to 10^{12.28} Pa s for temperatures varying from 639 to 719 °C (Fig. 3).

3.4. Low-temperature viscosity

Fig. 3 shows viscosity measurements performed with MP at T_{onset} (10 °C min⁻¹), T_{onset} (20 °C min⁻¹), or 50 °C above the T_{onset} (10 °C min⁻¹). For a given temperature and/or sample composition, the viscosity data are in good agreement with values derived by DSC within 10^{0.13} Pa s. The only exceptions are represented by the undoped sample C10M4 and the doped samples C18M5 and C13M8, where viscosity values are between ~10^{0.5} Pa s (C13M8 at 747 °C) and ~10^{1.3} Pa s (C10M4 at 730 °C) higher than those derived by DSC (Fig. 3).

3.5. Raman data

3.5.1. Raman spectra before DSC and MP measurements

Fig. 4 shows Raman spectra for undoped and doped samples. The spectral features can be categorized in three regions: 1) a low-frequency region (LF: ~250–600 cm⁻¹), 2) an intermediate-frequency region (IF: ~600–800 cm⁻¹), and 3) a high-frequency region (HF: ~800–1200 cm⁻¹).

In the LF region, Raman spectra for the undoped sample C10M4 (~10 wt% CaO and ~4 wt% MgO) and the weakly doped sample C18M5 (~18 wt% CaO and ~5 wt% MgO) show the highest intensity at ~500 cm⁻¹. In sample C13M8 (~13 wt% CaO and ~8 wt% MgO), the intensity at ~500 cm⁻¹ decreases. The same trend is observed in the highly doped samples C26M5 (~26 wt% CaO and ~5 wt% MgO) and C19M17 (~19 wt% CaO and ~17 wt% MgO), where the spectral intensity at ~500 cm⁻¹ decreases significantly. The centroid of Raman feature in the IF region shifts from 725 cm⁻¹ (undoped sample C10M4) to 695 cm⁻¹ (C17M5), namely with increasing the doping components.

Table 1

Microprobe analyses (wt%) of undoped (C10M4) and doped (C18M5, C26M5, C13M8 and C19M17) starting materials used in this study normalized to 100 %. σ represents the standard deviation of 10 microprobe analyses.

CaCO ₃ (wt%) added	14.00		30.00		7.00		20.00			
CaO (wt%) added	7.84		16.81		3.92		11.21			
MgO (wt%) added					5.00		15.00			
(wt%)	C10M4	σ	C18M5	σ	C26M5	σ	C13M8	σ	C19M17	σ
SiO ₂	50.76	0.19	46.12	0.37	41.49	0.36	46.67	0.35	38.80	1.05
TiO ₂	0.84	0.05	0.74	0.05	0.68	0.02	0.77	0.06	0.65	0.08
Al ₂ O ₃	17.47	0.11	15.62	0.17	13.66	0.11	15.90	0.14	12.95	0.47
FeO	6.03	0.18	5.50	0.13	4.81	0.10	5.46	0.11	4.92	0.10
MnO	0.14	0.03	0.13	0.03	0.12	0.03	0.12	0.03	0.12	0.04
MgO	4.00	0.07	4.50	0.15	4.91	0.09	8.29	0.48	17.02	1.81
CaO	10.08	0.18	18.09	0.77	26.35	0.52	13.10	0.37	19.15	0.46
Na ₂ O	2.95	0.08	2.60	0.11	2.20	0.06	2.68	0.05	1.82	0.18
K ₂ O	7.18	0.07	6.24	0.28	5.33	0.18	6.50	0.26	4.15	0.50
P ₂ O ₅	0.55	0.06	0.45	0.05	0.44	0.09	0.50	0.06	0.42	0.06
Total	100.00		100.00		100.00		100.00		100.00	

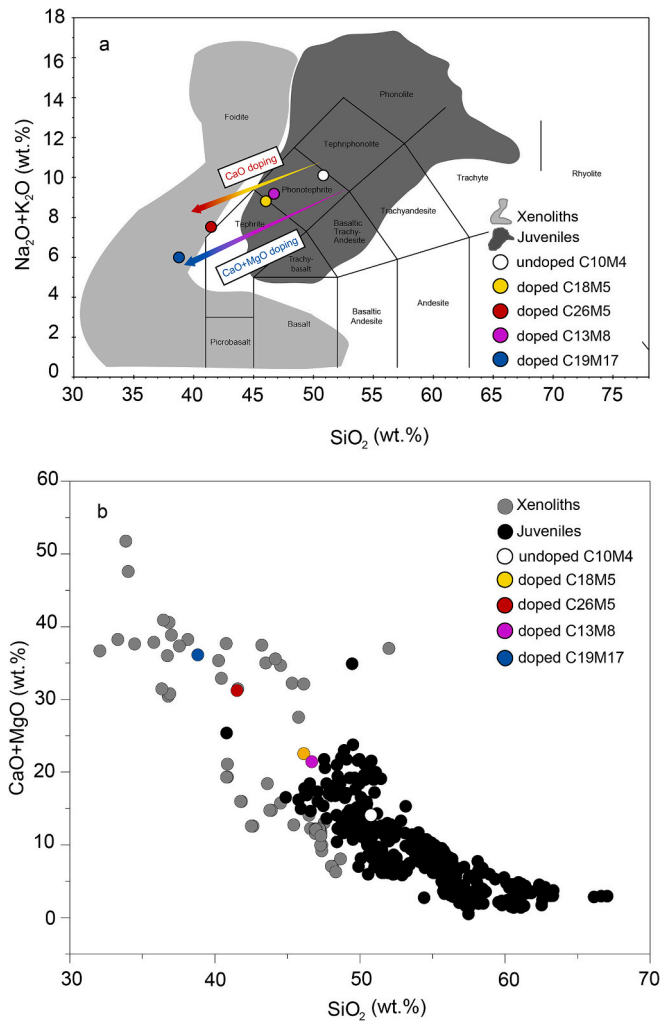


Fig. 1. a) Total alkali vs. silica (TAS) diagram showing the undoped and doped glass compositions used in this study. The undoped material (C10M4) is represented as the white symbol. CaO doped samples are represented by the yellow (C18M5) and red (C26M5) symbols, whilst purple (C13M8) and blue (C19M17) symbols correspond to samples doped with CaO and MgO. Areas represent the compositional variations of the products erupted from Vesuvius, specifically, the dark grey area represents juvenile materials (Jolis et al., 2015; Macdonald et al., 2016; Rosi and Santacroce, 1983; Santacroce et al., 2008), while the light grey area represents xenoliths (Del Moro et al., 2001; Fulignati et al., 2000, 2004; Jolis et al., 2015). The chemical compositions of this study are reported in Table 1. b) CaO + MgO vs. SiO₂ diagram displaying the erupted material (juvenile and xenoliths) from Vesuvius, undoped and doped glass composition used in this study. (For interpretation of the references to colour in this figure legend, the reader is referred to the web version of this article.)

Table 2

Viscosity measurements for all compositions at high temperatures by concentric cylinder (CC), reported with temperature.

C10M4		C18M5		C26M5		C13M8		C19M17	
<i>T</i>	$\log_{10} \eta$								
(°C)	(η in Pa s)								
1396	1.41	1400	0.36	1252	0.69	1398	0.81	1399	0.46
1350	1.63	1352	0.86			1350	1.08	1350	0.87
1301	1.91	1300	1.19			1325	1.25	1300	1.17
1276	2.06	1275	1.38			1300	1.38	1276	1.35
1251	2.21	1251	1.54			1275	1.51	1250	1.54
1226	2.37	1225	1.72			1251	1.63	1225	1.73
1201	2.54	1200	1.9			1225	1.78		
1176	2.71	1175	2.09			1200	1.96		
		1150	2.28						

The Raman band in the HF region of the undoped sample C10M4 is symmetric and centred at $\sim 960 \text{ cm}^{-1}$ but, as the doping level increases in the two different series, the band shifts to lower wavenumbers and becomes asymmetric due to the development of a shoulder at $\sim 885 \text{ cm}^{-1}$.

3.5.2. Raman spectra after DSC and MP measurements

Fig. 5 illustrates Raman spectra for doped and undoped glasses before (untreated) and after DSC (Fig. 5a-e) and MP (Fig. 5f-l) viscosity measurements (treated). For the undoped sample C10M4 (Fig. 5a), the Raman intensity of DSC-treated glasses at approximately $\sim 500 \text{ cm}^{-1}$ increases and slightly shifts to lower wavenumbers with decreasing $q_{c,h}$ from 20 to 5 °C min⁻¹, mainly in response to the time spent in the undercooled liquid state. LF Raman spectra of CaO-doped samples C18M5 and C26M5 show no changes (Figs. 5b, c). However, the HF band shifts to lower wavenumbers for sample C26M5 and becomes asymmetric due to the development of a shoulder at $\sim 885 \text{ cm}^{-1}$ (Fig. 5c). For the poorly CaO + MgO-doped sample C13M8 (Fig. 5d), the intensity of DSC-treated glass at $\sim 500 \text{ cm}^{-1}$ slightly increases compared to the untreated glass. For sample C19M17 doped with the highest MgO content (Fig. 5e), the HF band centroid shifts from $\sim 940 \text{ cm}^{-1}$ (untreated glass) to $\sim 925 \text{ cm}^{-1}$ (DSC-treated glass) for measurements at $q_{c,h}$ of 20 °C min⁻¹. Raman spectra of DSC-treated glasses measured at $q_{c,h}$ of 10 and 5 °C min⁻¹ resemble that of the untreated glass.

Fig. 5f shows Raman spectra of untreated and MP-treated glasses for

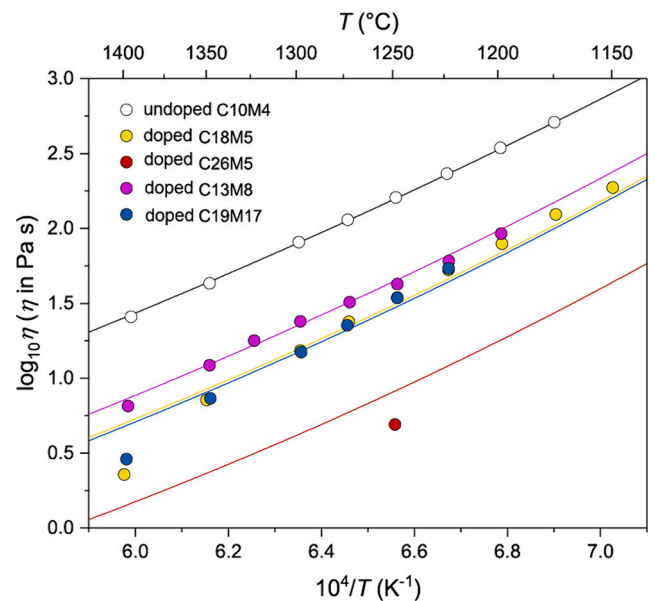


Fig. 2. High-temperature viscosity measured with a concentric cylinder apparatus. Curves correspond to MYEGA fits from Eq. (5) (See Section 4.2).

Table 3

Low temperature viscosity data derived by DSC at the characteristic temperatures. The symbol “*” indicates viscosities measured by MP.

Sample		T_5 onset	T_{10} onset	T_{20} onset	T_5 peak	T_{10} peak	T_{20} peak	T_{10} peak+50
C10M4	°C	639	643	652	674	678	694	730
	$\log_{10} \eta$ (η in Pa s)	12.28	11.98	11.68	10.92	10.62	10.32	–
C18M5	°C	660	667	672	694	704	709	754
	$\log_{10} \eta$ (η in Pa s)	12.28	11.98	11.68	10.92	10.62	10.32	–
C26M5	°C	670	674	680	702	710	719	760
	$\log_{10} \eta$ (η in Pa s)	12.28	11.98	11.68	10.92	10.62	10.32	–
C13M8	°C	655	659	668	691	698	708	747
	$\log_{10} \eta$ (η in Pa s)	12.28	11.98	11.68	10.92	10.62	10.32	–
C19M17	°C	663	665	676	696	704	714	753
	$\log_{10} \eta$ (η in Pa s)	12.28	11.98	11.68	10.92	10.62	10.32	–
		–	–	–	–	10.91*	–	8.62*

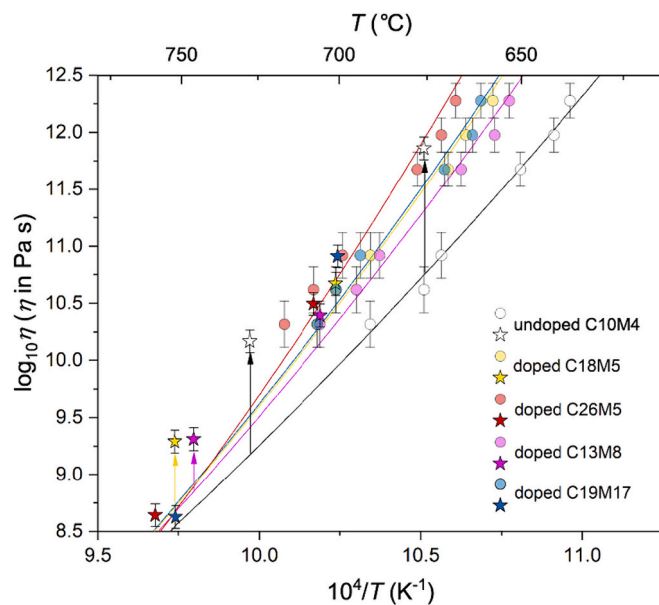


Fig. 3. Low-temperature viscosity derived by DSC (circles) and measured using MP (stars). Curves correspond to MYEGA fits of DSC data from Eq. (5). See Section 4.2.

C10M4. As the temperature of viscosity measurement increases ($T_{peak10} = 678$ °C and $T_{peak10+50} = 730$ °C), the intensity at ~ 500 and ~ 960 cm^{-1} also increases. The inspection of Raman spectra for the poorly CaO-doped sample C18M5 (Fig. 5g) reveals that at the lowest temperature ($T_{peak10} = 704$ °C) the intensity at ~ 500 cm^{-1} increases. The Raman spectrum of the MP-treated glass at the highest temperature (T_{peak10} of 754 °C) shows a similar increase at ~ 500 cm^{-1} and the intensity also increase at ~ 700 cm^{-1} . Fig. 5h illustrates Raman spectra of the untreated and MP-treated glasses from the highly CaO-doped sample C26M5. Raman spectra of MP-treated glasses ($T_{peak10} = 710$ °C and $T_{peak10+50} = 760$ °C) exhibit a subtle intensity increase at ~ 500 cm^{-1} . Raman spectra of the MP-treated glasses from the lowest CaO and MgO-doped sample C13M8 ($T_{peak20} = 708$ °C and $T_{peak10+50} = 747$ °C) exhibit an increase at ~ 500 cm^{-1} (Fig. 5i). Additionally, the Raman spectrum of MP-treated glass at $T_{peak10+50}$ of 747 °C shows an increase in the intensity at ~ 690 cm^{-1} . Finally, Raman spectra of the MP-treated glasses from the highly CaO and MgO-doped C19M17 ($T_{peak10} = 704$ °C and $T_{peak10+50} = 753$ °C) indicate no structural changes (Fig. 5l).

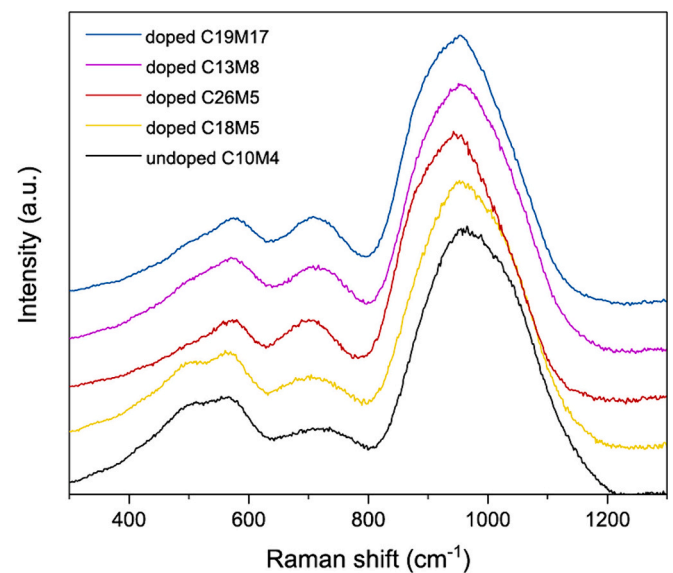


Fig. 4. Raman spectra of the undoped (C10M4) and doped (C18M5, C26M5, C13M8, and C19M17) samples.

3.6. Brillouin spectroscopy

The longitudinal sound velocity (V_p) increases with increasing both CaO and CaO + MgO doping levels, ranging from 6039.9 to 6498.5 m/s. The shear sound velocity (V_s) shows a less pronounced increase which mirrors the trend observed in V_p . The calculated ratio of elastic moduli K/G from Eq. (3) for the undoped sample C10M4 is 1.64, while for low and high doping levels the magnitude increases to 1.76 and 1.89, respectively.

The melt fragility m calculated using Eq. (4) (Angell, 1995; Plazek and Ngai, 1991) has been obtained after Cassetta et al. (2021) and reported in Table 4. The undoped sample C10M4 is characterized by a lower melt fragility (~ 40) that increases up to ~ 44 for low doped CaO (C18M5) and CaO + MgO (C13M8) samples, and up to ~ 50 for the high doped (C26M5 and C19M17) samples.

4. Discussion

4.1. Viscosity data evaluation

During MP and DSC measurements, the melt might undergo nanocrystallization or, alternatively, might develop a heterogeneous nanostructure (Bouhifd et al., 2004; Di Genova et al., 2020; Di Genova et al.,

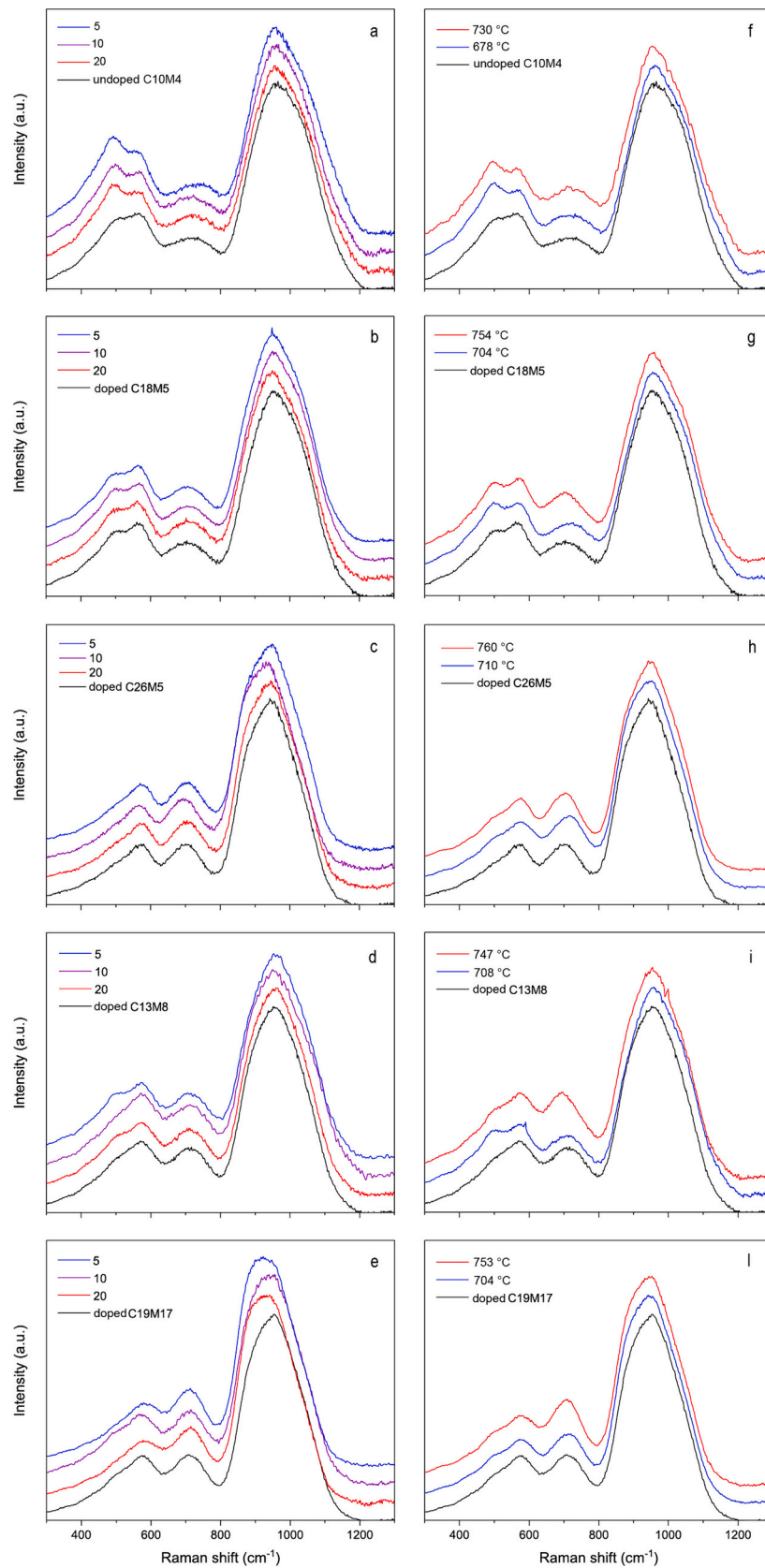


Fig. 5. Baseline-corrected and normalized Raman spectra. Left panels (a-e) show Raman spectra of untreated (black) and DSC-treated glasses (number in the legend indicates $q_{c,h}$). Right panels (f-l) show Raman spectra of untreated (black) and MP-treated glasses at different target temperatures.

Table 4Measured longitudinal (V_p) and shear (V_s) sound velocity, glass density (ρ), calculated bulk (K) and shear (G) moduli, and melt fragility calculated m from Eq. (4).

Sample	V_p (m/s)	V_s (m/s)	ρ g/cm ³	K GPa	G GPa	K/G	m
C10M4	6039.88 ± 20.71	3502.75 ± 5.56	3.06	0.06155	0.03753	1.64 ± 0.02	39.61 ± 0.48
C18M5	6176.13 ± 21.12	3512.13 ± 11.57	2.06	0.04462	0.02536	1.76 ± 0.03	44.76 ± 0.76
C26M5	6326.50 ± 23.43	3526.25 ± 15.32	2.59	0.06079	0.03224	1.89 ± 0.04	50.24 ± 0.97
C13M8	6222.25 ± 11.19	3540.38 ± 8.43	2.05	0.04515	0.02572	1.76 ± 0.02	44.61 ± 0.46
C19M17	6498.50 ± 10.28	3620.88 ± 9.36	2.33	0.05768	0.03055	1.89 ± 0.02	50.34 ± 0.52

2017b; Liebske et al., 2003; Okumura et al., 2022; Valdivia et al., 2023; Verdurme et al., 2023). Thus, it is essential to investigate the glass used for MP and DSC analyses by Raman spectroscopy before and after the measurements. Failing to do so may result in data not accurately representing the viscosity of the melt phase but rather that of a heterogeneous material at the nanoscale measurements (Di Genova et al., 2020; Scarani et al., 2022b; Valdivia et al., 2023; Zandonà et al., 2023).

In the case of the undoped sample C10M4, Fig. 3 shows that the viscosity measured ($10^{11.86}$ Pa s) by MP at 678 °C (T_{peak10}) is $10^{1.24}$ Pa s higher than the viscosity measured by DSC at the same temperature. This discrepancy raises concerns about the potential effect of nanocrystallization during the viscosity measurement. Otherwise, it prompts questions about the reliability of the chemically independent DSC approach used to derive the viscosity (Gottsmann et al., 2002), suggesting that the K_{onset} and K_{peak} selected here may be not correct. The close examination of Raman spectra not only reveals structural modifications during high temperature MP measurements (Fig. 5f) but also during DSC measurements (Fig. 5a). The increase in the intensity at ~ 485 cm⁻¹ in the LF region suggests the formation of oxygen atoms arranged in four-membered rings with breathing motion perpendicular to the Si-O-Si plane (Galeener, 1982; Le Losq and Neuville, 2013; Pasquarello and Car, 1998; Rahmani et al., 2003; Sharma et al., 1981). Thus, we infer that structural reorganization occurred in the undoped C10M4 melt during both MP and DSC measurements, possibly resulting in the formation of new four-membered rings of tetrahedra. Despite the similarity between Raman spectra from MP measurements (Fig. 5f) and those obtained after DSC measurements (Fig. 5a), the viscosity measured by MP is least 1 log unit higher than the DSC-derived viscosity (Fig. 3). We posit that the formation of new tetrahedral rings markedly increases the relaxation timescale of the melt when subjected to shear deformation during MP measurements. Conversely, DSC measurements, relying on a bulk property, does not appear to be significantly affected by these local structural changes. However, we also tested the hypothesis proposed by Gottsmann et al. (2002) that K_{peak} depends on composition, which means that the DSC-derived values may shift to lower or higher values. Gottsmann et al. (2002) showed that K_{peak} decreases from 10.8 (in the rhyolite domain) to 9.64 (in basanite), and this behaviour was parameterized using the empirical parameter E.O. (excess of oxide, in mol%; Table S2). This parameter is calculated by subtracting the sum of the molar percentages of Al₂O₃, TiO₂, and 0.5FeO (considered structural network formers) from the sum of the molar percentages of oxides regarded as network modifiers (0.5FeO, MnO, MgO, CaO, Na₂O, K₂O, P₂O₅ and H₂O). Using this parameterization, we found that K_{peak} ranges from 9.85 for our undoped melt sample (C10M4, E.O. = 14.93) to 9.67 for the highly Ca–Mg doped melt sample (C19M17, E.O. = 41.78) (Table S2). Notably, as reported in Section 2.5, we use a K_{peak} value of 9.84 ± 0.20 (Di Genova et al., 2020), which falls within the range calculated using the method of Gottsmann et al. (2002) (Table S2). Therefore, even if we assume that K_{peak} depends on chemical composition, our assumption of a constant K_{peak} value, as presented in our manuscript, holds true for the chemical landscape explored in this study.

The reliability of our DSC approach can be validated by examining the viscosity data of doped samples (Fig. 3). Viscosity data measured at T_{peak10} and T_{peak20} by using MP match those derived by the DSC-derived viscosity within the experimental error, provided that Raman spectra of

glasses remain unchanged after MP measurements (Fig. 5g-l). As for the C10M4 sample, the viscosity of doped melts was also measured at $T_{peak+50}$. Raman spectra of some post MP measurements exhibit features indicative of various degrees of structural changes (Fig. 5g-l), whose overall entity, even if smaller than those exhibited by the undoped C10M4 sample (C18M5 at 704 and 754 °C, C13M8 at 708 and 747 °C), renders them inappropriate to be used for viscosity calculation. Therefore, DSC data either in conjunction with or as an alternative to MP measurements, are deemed more appropriate for modelling the viscosity change with temperature. However, given the restricted viscosity-temperature interval explored by DSC measurements, an accurate extrapolation of the DSC-derived viscosity at higher temperature is essential. Consequently, we present viscosity models for our melts that facilitate the calculation of viscosity over a wide temperature range.

4.2. Modelling melt viscosity and melt nanoheterogeneity effect

CC and DSC viscosity data were fitted by employing the Mauro-Yue-Ellison-Gupta-Allan (MYEGA) equation (Mauro et al., 2009) that uses viscosity at infinite temperature ($\log_{10}\eta_{\infty}$), glass transition temperature (T_g) and melt fragility (m) as parameters:

$$\log_{10}\eta_s(T) = \log_{10}\eta_{\infty} + (12 - \log_{10}\eta_{\infty}) \frac{T_g}{T} \exp \left[\left(\frac{m}{12 - \log_{10}\eta_{\infty}} - 1 \right) \left(\frac{T_g}{T} - 1 \right) \right] \quad (5)$$

The viscosity at infinite temperature was set to -2.93 (Cassetta et al., 2021; Langhammer et al., 2021, 2022; Zheng et al., 2011), while T_g and m were set as fit parameters. Results from calculations are reported in Table 5, while the temperature-dependence of the viscosity is illustrated in Fig. 6.

Broadly, the inspection of m in Table 5 reveals that the melt fragility increases from 35.9 to 50.0 with increasing the addition of doping oxides for the two doped series, which results in the increase of the non-Arrhenian behaviour in Fig. 6. With respect to the undoped C10M4 composition, the melt exhibits lower viscosity at high temperature and vice versa when the doping oxide concentration increases, thereby leading to a viscosity-temperature crossover at ~ 750 °C (Fig. 6).

The modelling of melt viscosity and the analysis of Raman spectra post MP measurements enable the accurate evaluation of the viscosity increase due to formation of nanoheterogeneities especially at $T_{peak+50}$, where the DSC-derived viscosity cannot be obtained. As discussed above, MP data of the undoped C10M4 melt exhibit the highest deviation in viscosity from the DSC-derived viscosity and thus the MYEGA fit (Fig. 3). The viscosity increases by 13-fold ($10^{1.11}$ Pa s) at T_{peak10} of 678 °C and 10-fold ($10^{1.01}$ Pa s) at $T_{peak10+50}$ of 730 °C. We argue that the

Table 5
MYEGA fit parameters obtained from Eq. (5).

	C10M4	C18M5	C26M5	C13M8	C19M17
$\log_{10}\eta_{\infty}$	-2.93	-2.93	-2.93	-2.93	-2.93
T_g (°C)	643.87 ± 0.58	667.28 ± 1.20	677.15 ± 2.1	662.24 ± 0.84	668.20 ± 1.16
m	35.92 ± 0.14	43.50 ± 0.39	49.96 ± 2.31	41.70 ± 0.27	43.77 ± 0.46
RMSE	0.04	0.11	0.19	0.07	0.12

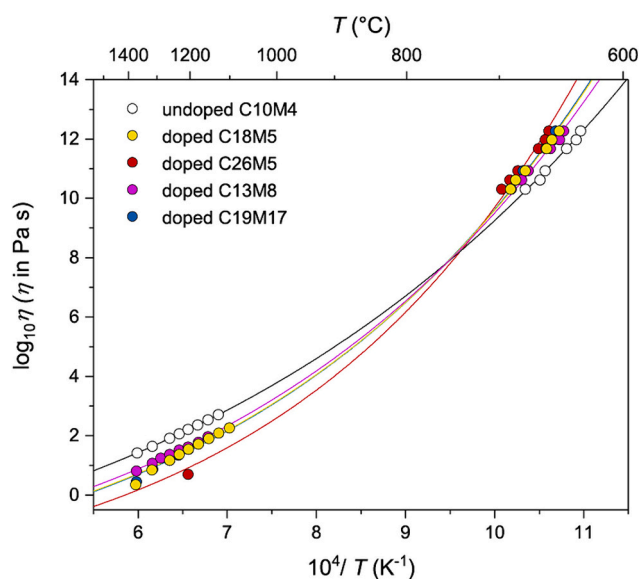


Fig. 6. Viscosity data from DSC and CC measurements, and MYEGA fits obtained by using Eq. (5).

increase in viscosity is related to the formation of new four-membered rings of tetrahedra (Fig. 5f). For the doped sample C18M5, the viscosity measured at $T_{peak10+50}$ of 754 °C deviates $10^{0.59}$ Pa s (~ 4 -fold) from the MYEGA fit (Fig. 3). Coherently, the Raman spectrum of the post viscosity measurement glass shows an increase in intensity at ~ 700 cm^{-1} , also accompanied by the shift of the HF band centroid position from ~ 940 to ~ 920 cm^{-1} (Fig. 5b). Based on Raman literature of volcanic glasses (Di Genova et al., 2016, 2017b; Di Muro et al., 2009; Schiavi et al., 2018; Wang et al., 1993, 1995), we state that this sample underwent nanostructure due to Fe–Ti clustering (intensity increase at ~ 700 cm^{-1}) and possibly iron oxidation (HF centroid shift). Moreover, the increase in the intensity of Raman spectra at ~ 500 and ~ 690 cm^{-1} for the doped sample C13M8 at T_{peak20} of 708 °C and $T_{peak10+50}$ of 747 °C (Fig. 5i), respectively, is correlated with a departure of the measured viscosity from the MYEGA fit ($10^{0.23}$ Pa s and $10^{0.47}$ Pa s, respectively). For the measured viscosities that align with the MYEGA fit (Fig. 3), Raman spectroscopy results confirm that no major changes occurred during the measurement (Fig. 5).

In summary, our integrated approach employing DSC for deriving melt viscosity, MP for measuring the viscosity of nanoheterogeneous melts, and Raman spectroscopy for detecting nanoheterogeneities provides a robust tool to quantify the viscosity increase attributed to nanoscale melt structural modifications. In the following, we discuss the possible melt structural changes occurred in our sample due to the addition of alkaline earth cations. Next, we explore the predictive capability of empirical models from literature, in which the integrated approach presented in this study has been sporadically employed by previous authors (Al-Mukadam et al., 2020; Di Genova et al., 2020; Stabile et al., 2021; Valdivia et al., 2023; Zandonà et al., 2023).

4.3. Structural role of alkaline earth cations

The finding that CaO alone reduces viscosity at high temperatures more effectively than CaO combined with MgO might seem counterintuitive (Richet et al., 2009). Moreover, we observe no apparent relationship between viscosity reduction and NBO/T or between NBO/T and fragility of the melt (Figs. S4 and S5). The most depolymerized melt (C19M17) has in fact an intermediate calculated fragility ($m = 43.77$) and intermediate viscosity, both at high and low temperature (Fig. 3). The fragility and the viscosity trends seem however being related to the total Ca content in both series, regardless of the Mg content.

Fragility increases with increasing CaO content and, at high temperatures, viscosity follows the opposite trend. However, this trend reverses at low temperatures. Surprisingly, MgO addition has minimal impact on viscosity despite its network-modifying role. This contradicts the expectation of lower viscosity with increased network modifiers, especially at high temperatures. Additionally, the combined effect of CaO and MgO was not observed to further decrease low-temperature viscosity.

It is generally assumed as the concentration of network modifiers cations (Ca^{2+} and Mg^{2+}) increases, the melt polymerization is expected to decrease according to the following exchange reactions: 1) $\text{Si-O-Si} + \text{Ca-O-Ca} \leftrightarrow 2\text{Ca-O-Si}$ and 2) $\text{Si-O-Si} + \text{Mg-O-Mg} \leftrightarrow 2\text{Mg-O-Si}$. We propose that ionic potential of Mg^{2+} and competition with Ca^{2+} cations for bonding with oxygen limit the ability of MgO addition to break down the network (depolymerize) shifting the Eq. (2) to the left. This explains the minimal viscosity change observed with MgO addition, both at high and low temperature. This findings align with the observation of Dingwell et al. (1996) that Mg^{2+} cations have a weaker effect on viscosity compared to other network modifiers.

The crossover of the viscosity curves at $T \approx 750$ °C leads to changes in the viscosity versus composition relationships. In particular, the increase in viscosity for doped melts compared to undoped at low temperature presents a distinct feature. However, at low temperature, the different contribution of chemical versus topological terms of the configuration entropy may lead to these unexpected trends, as exemplified in the findings of Giordano et al. (2009).

In conclusion, the role of MgO addition in the melt structure appears to be more complex than previously thought, requiring further investigation for the interplay between cationic potential and network interactions in multicomponent melts.

4.4. Comparison with models from literature

The viscosity data set obtained from this study has been compared with predictions of empirical models from literature: 1) the chemically-based GRD and LDS models from Giordano et al. (2008) and Langhammer et al. (2022), and 2) the Brillouin spectroscopically-based BLS model from Cassetta et al. (2021). For this comparison, we used only data from glasses unaffected by structural changes after the viscosity measurement, as revealed by Raman spectroscopy. The root-mean square error (RMSE) calculated for each tested model is reported in Table 8.

The GRD model relies on the Vogel-Fulcher-Tamman (VFT) equation and has been calibrated with the viscosity at infinite temperature ($\log_{10}\eta_{\infty}$) equal to -4.55 , while both LDS and BLS models describe the temperature-dependence of melt viscosity according to the MYEGA fit from Eq. (5) and they assume $\log_{10}\eta_{\infty}$ equal to -2.93 (Langhammer et al., 2022; Mauro et al., 2009; Zheng et al., 2011). For the BLS model, m was derived by using Eq. (4) and T_g via DSC measurements (see $T_{onset10}$ in Table 3).

The BLS model performs the best in predicting viscosity for all the five samples across the entire temperature interval (i.e., HT and LT data). For example, RMSE_{BLS} , RMSE_{GRD} , and RMSE_{LDS} of the undoped C10M4 sample are 0.44, 0.83, and 0.98, respectively (Table 6). Collectively, these three models return similar estimates for the viscosity of low doped C18M5 ($\text{RMSE}_{\text{BLS, GRD, LDS}} \approx 0.19$) and C13M8 ($\text{RMSE}_{\text{BLS, GRD, LDS}} \approx 0.29$) samples. However, when considering the high doped C26M5

Table 6

Root mean square error (RMSE) of GRD (Giordano et al., 2008), LDS (Langhammer et al., 2022) and BLS (Cassetta et al., 2021) viscosity models.

	C10M4	C18M5	C26M5	C13M8	C19M17
GRD	0.83	0.19	0.55	0.26	1.35
LDS	0.98	0.23	1.18	0.30	1.00
BLS	0.44	0.16	0.26	0.31	0.56

and C19M17 samples, the BLS model significantly performs better ($RMSE_{BLS} = 0.26$ and 0.56 , respectively) than the GRD ($RMSE_{GRD} = 0.55$ and 1.35 , respectively) and LDS ($RMSE_{LDS} = 1.18$ and 1.00 , respectively) models (Table 6). This finding outlines the restricted applicability of chemical-based models to compositional domains beyond their calibration data sets (Fig. S3). We propose that the BLS model exhibits superior performance because, unlike for the GRD and LDS models, the T_g is measured via DSC and the input data are filtered to exclude viscosity measurements influenced by nanocrystallization (e.g., Di Genova et al., 2020) and/or melts depletion in Fe and Ti (e.g., Hushur et al., 2013; Richet et al., 1996; Richet and Polian, 1998; Whittington et al., 2001, 2012).

As a further test, we closely examine the data sets used to calibrate the GRD and LDS models, which also include phonotephritic compositions. To validate our observations, we compare the viscosity data of our undoped C10M4 sample with literature data from Giordano and Dingwell (2003). The authors measured the viscosity of the sample Ves_G_tot with composition nearly identical to that used in this study. The main compositional difference regards the FeO_{tot} content, as sample C10M4 has 6.03 wt% FeO_{tot} and sample Ves_G_tot has 7.20 wt% FeO_{tot} . Given the higher FeO_{tot} , lower viscosity for sample Ves_G_tot is expected (Di Genova et al., 2017a, 2017b; Valdivia et al., 2024). Fig. 7 shows that the Ves_G_tot melt is indeed less viscous in the high-temperature regime, with a viscosity of $\sim 10^{1.3}$ Pa s at ~ 1347 °C, compared to our melt, which is $\sim 10^{0.3}$ Pa s more viscous at the same temperature. However, sample Ves_G_tot reaches higher viscosity values in the low-temperature regime, where structural changes can easily occur (Fig. 3). For example, the Ves_G_tot sample has a viscosity of $\sim 10^{11}$ Pa s at 696 °C, while sample C10M4 is $10^{0.6}$ Pa s less viscous. Moreover, MP viscosity measured at 730 °C ($T_{peak10+50}$) for sample C10M4, where Raman spectroscopy reveals structural modification during the measurement (Fig. 5f), aligns with Ves_G_tot viscosity. As emphasized in emerging literature (Di Genova et al., 2017a,b, 2020; Scarani et al., 2022a, 2022b; Valdivia et al., 2023; Verdurme et al., 2023), we underscore the importance of rigorously testing empirical viscosity models before their application to natural environments, especially considering structural changes occurring at low-temperature measurements.

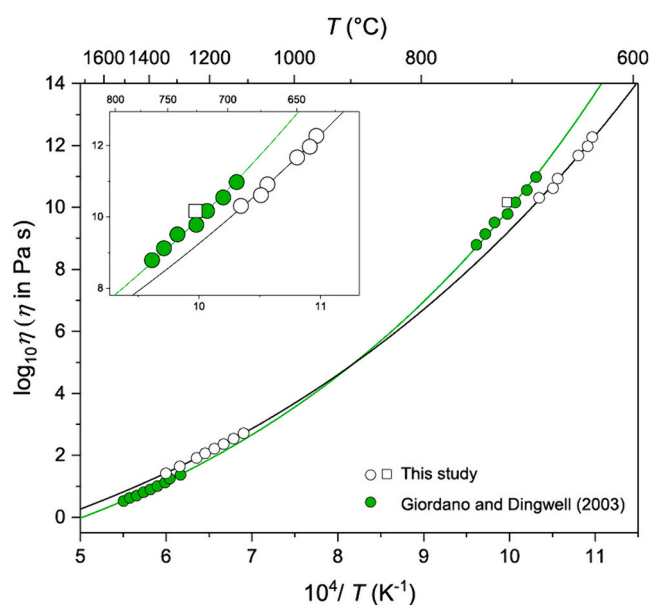


Fig. 7. Viscosity data for phonotephritic melts. White circles are viscosities of sample C10M4 derived by CC and DSC, while the white squares refer to MP measurements. Green symbols are viscosity data from Giordano and Dingwell (2003). MYEGA fits of viscosity data are also shown in figure as black and green curves. (For interpretation of the references to colour in this figure legend, the reader is referred to the web version of this article.)

By employing MYEGA parameterizations (Fig. 6 and Table 5), we computed the viscosity resulting from the addition of only CaO or from the addition of CaO + MgO, focusing on three temperature conditions where substantial and contrasting effects were found (Fig. 8): i) a high- T region ($T = 1000$ °C), ii) an intermediate- T region ($T = 750$ °C), and iii) a low- T region ($T = 666$ °C). As shown in Fig. 6, in the high- T region all doped melts display lower viscosity compared to the undoped melt, whereas the opposite behaviour is encountered in the low- T region. The contrasting behaviour at high- and low- T in the studied melts results in a series of crossover in the viscosity curves. Notably all crossovers occur in a very narrow T range, around $T = 750$ °C, at which viscosity variation is minimal across all samples.

In the high- T regime (Fig. 8a), results indicate that the addition of CaO induces more significant viscosity decrease compared to the addition of CaO + MgO. Specifically, addition of ~ 17 wt% CaO results in nearly a 13-fold viscosity decrease ($10^{1.11}$ Pa s), while addition of ~ 11 wt% CaO and 15 wt% MgO leads to a nearly 4-fold viscosity decrease ($10^{0.58}$ Pa s). Notably, the viscosity models of GRD (Giordano et al., 2008), LDS (Langhammer et al., 2022) and BLS depict a different behaviour (Fig. 8d), predicting the highest viscosity reduction in the case of melts doped with CaO + MgO. For instance, the GRD model predicts a decrease in viscosity of nearly a 400-fold with the addition of ~ 11 wt% CaO and ~ 15 wt% MgO which is 100-fold higher than our measurements, and a decrease in viscosity of nearly a 60-fold with the addition of ~ 17 wt% CaO.

The opposite trend is observed in the low- T region (Fig. 8c), where doping always induces an increase of viscosity compared to the undoped melt. Furthermore, the addition of CaO alone induces a higher viscosity increase compared to the addition of similar amounts of CaO + MgO. Specifically, our modelling shows that the addition of ~ 17 wt% CaO results in the highest viscosity, with nearly a 28-fold increase ($10^{1.45}$ Pa s) with respect to the undoped material, while addition of ~ 11 wt% CaO and 15 wt% MgO leads to a nearly ~ 9 -fold increase in viscosity ($10^{0.94}$ Pa s). This trend is not captured by GRD and LDS models (Fig. 8f) that predict the highest viscosity for the undoped melt, up to $10^{1.42}$ Pa s higher than estimates derived from our model (Fig. 8c). This inconsistency reflects in an apparent, though inaccurate, opposite effect induced by the doping with CaO and CaO + MgO, leading to a decrease in viscosity in the low- T region.

Finally, it is worth noting that the temperature ($T = \sim 750$ °C) at which our data and modelling indicate a convergence of all curves at $\sim 10^{8.7}$ Pa s (Fig. 8b), appears to be a characteristic feature that is not reproduced by any of the chemical-based models (GRD and LDS; Fig. 8e).

4.5. Implications for magma dynamics and xenoliths preservation

Magma-carbonate interaction is well-documented in geological records (see Knuever et al., 2023a for a review) across various volcanic systems such as Vesuvius (Barberi and Leoni, 1980; Bruno et al., 1998; Dallai et al., 2011; Fulignati et al., 2000, 2004; Gilg et al., 2001; Iacono Marziano et al., 2007b, 2008; Jolis et al., 2013, 2015; Stabile and Carroll, 2019), Colli Albani (Di Battistini et al., 1998, 2001; Di Rocco et al., 2012; Di Stefano et al., 2018; Freda et al., 2008; Gaeta et al., 2009; Gozzi et al., 2014; Iacono Marziano et al., 2007a; Kleest et al., 2020; Kleest and Webb, 2021, 2022; Mollo and Vona, 2014), and Mt. Etna (Chiodini et al., 2011; Michaud, 1995; Mollo et al., 2011, 2012; Villemant et al., 1993) in Italy, Merapi in Indonesia (Chadwick et al., 2007; Troll et al., 2012) and Popocatepetl, Mexico (Goff et al., 2001; Schaaf et al., 2005). Our research establishes the groundwork for measuring the influence of carbonate assimilation on magma viscosity, mostly concentrating on the straightforward scenario of anhydrous chemical compositions. Nevertheless, while this limitation is present at the laboratory scale, it is somewhat offset by two factors: 1) the relative low amount of H_2O that can be dissolved in melts forming in CO_2 -saturated magmatic reservoirs, and 2) the observation that both the increase of H_2O and T contribute to

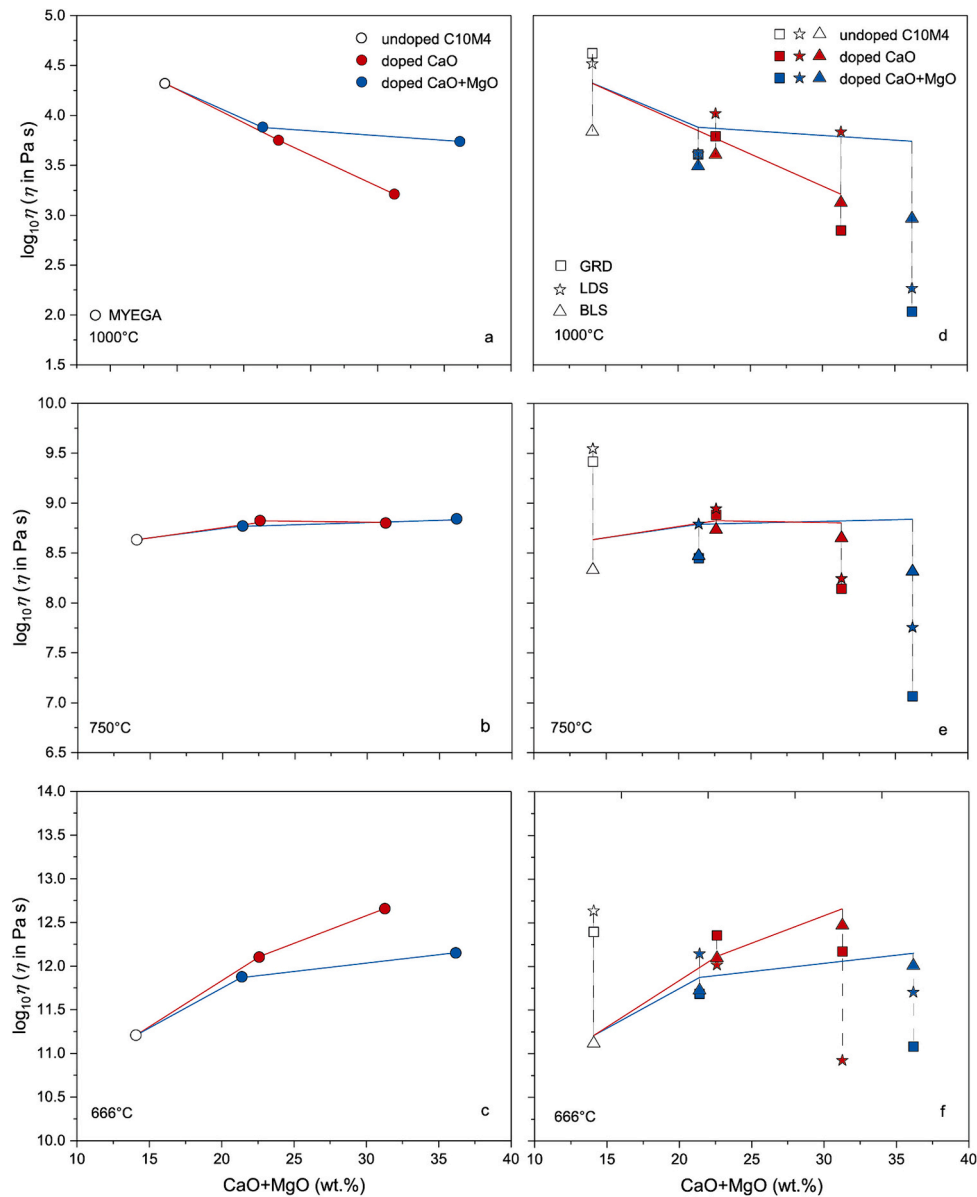


Fig. 8. Melt viscosities defined at three different target temperatures of 1000, 750 and 666 °C. Viscosities are computed by the GRD (square), LDS (star) and BLS (triangle) models and analysed as a function of CaO + MgO in wt%. Solid lines depict the viscosity trend of the CaO and CaO + MgO series, while dashed lines illustrate the deviation between the viscosity trend calculated by employing MYEGA parameterizations and the GRD, LDS and BLS models.

lowering the viscosity of the melt in the same direction. Specifically, our data allow to discuss the mobility and the mixing capability of melts subjected to different degrees of carbonate assimilation.

At Vesuvius, the magma chamber feeding the Pollena eruption was estimated to be at relatively shallow depth (3–4 km; Scaillet et al., 2008) within a thick calcite- and dolomite-bearing carbonate crust (Bruno et al., 1998; Cioni et al., 1998; Del Moro et al., 2001; Fulignati et al., 2004; Iacono Marziano et al., 2007b, 2008; Jolis et al., 2013, 2015; Sulpizio et al., 2005, 2007; Vona et al., 2020). According to the evolution trend inferred by Cioni et al. (1998) at Vesuvius, the magma chamber feeding Pollena eruption was in a “young” stage, typical of subplinian eruptive activity, characterized by a continuous thermal (T ranging from 850 to 1120 °C) and compositional gradients from a colder and evolved phonolite magma at the top to a hotter and more mafic phonotephritic magma at the bottom. Fulignati et al. (2004) interpreted the occurrence of xenoliths (i.e. clinopyroxenites, glass-bearing fergusites and foid-bearing syenites) in Pollena eruptive products as preservation of the magma chamber solidification front. Beyond the

solidification front, endoskarns or magmatic skarns formed at $T < 1000$ °C (melilite-bearing endoskarns) or $T < 800$ °C (phlogopite-bearing endoskarns), as the result of crystallization from Ca- and/or Mg-enriched melts, whose compositions results from the mixing of silicate melts with different amounts of CaO and MgO derived from the host carbonates (Knuever et al., 2023a).

As shown in Fig. 1, the compositions of our undoped and doped melts explore the same compositional range described by a mixing line connecting Vesuvius juvenile products (representing the “normal” composition of vesuvian magmas) to the most Ca-Mg-rich residual glasses of the endoskarn xenoliths. Therefore, our data set allows to track the rheological behaviour in an ideal profile along the chamber solidification and assimilation front towards the carbonate host rocks, starting from the pristine tephriphonolite melt (C10M4). In such a scheme, experimental CaO- and CaO-MgO-doped melts mimic hybrid melts that have undergone variable degrees of carbonate (calcite to dolomite) assimilation at different distance from the carbonate host.

The effects of carbonate assimilation are not limited to the magma

chamber walls but can pervade throughout. For instance, Jolis et al. (2015) showed that crystals in Vesuvius eruptive materials frequently exhibit elevated isotopic ratios of $\delta^{18}\text{O}$ (~7–11 ‰), indicating assimilation of carbonate wall-rocks with high $\delta^{18}\text{O}$ -values (~28–33 ‰). This suggests either widespread carbonate assimilation affecting significant portions of the stored magmas, or highly efficient mixing between contaminated magmas forming at the chamber margins and the residual pristine magma (Knuever et al., 2023a).

Several studies explored the rheological constraints on the magma mixing process (see Morgavi et al., 2022 for a recent review). Magma mixing occurs more efficiently when the viscosity difference between the end-member magmas is low, whereas for a higher viscosity contrast, magmas are only mechanically mixed (i.e., magma mingling) and do not form compositionally hybrid melts (Davi et al., 2009; Huppert et al., 1984; Sparks and Marshall, 1986). In the present study, we observe a very narrow range of temperature ($T \approx 750$ °C) at which anhydrous viscosity of all studied composition converge (i.e. $\eta \approx 10^{8.7}$ Pa s). Such a critical T , termed “inversion temperature” (T_i , after Fernandez and Gasquet, 1994) could delineate optimal conditions for the mixing of magmas undergoing variable degrees of carbonate assimilation, potentially generating a broad spectrum of hybrid compositions. Similarly, this minimal viscosity contrast may facilitate rapid carbonate assimilation during magmatic stoping, a process believed to produce significant CO_2 fluid, enhancing the eruption explosivity (Buono et al., 2020; Knuever et al., 2023c).

At $T > T_i$, CaO and CaO-MgO-rich magmas are the less viscous than undoped phonotephrite, whereas at $T < T_i$ these magmas become more viscous. The rheological behaviour of CaO-MgO-enriched melts compared to pristine melts resembles the injection of a mafic melt into a more felsic host magma. In that case, many studies (e.g., Davi et al., 2009; Fernandez and Gasquet, 1994) have shown that mixing occurs when the mafic end-member is less viscous than the felsic one, while the opposite case leads to mingling and the preservation of mafic enclaves. Similar rheological constraints may apply to melts undergoing different degrees of carbonate assimilation, where CaO-MgO-enriched melts efficiently mix with the host magma at $T > T_i$, while CaO-MgO-enriched melts are preserved as CaO-MgO-rich enclaves (i.e. endoskarn xenoliths) at lower temperatures.

It is crucial to note that our data, measured on nominally anhydrous melts, can only be qualitatively applied to natural settings. For instance, the absolute value of viscosity at the inversion temperature ($\eta > 10^5$ Pa s) would be too high to allow magma mixing (Morgavi et al., 2022; Woods and Cowan, 2009). The water content in pre-eruptive Pollena magmas, estimated at 3–5 wt% by Fulignati and Marianelli (2007) through melt inclusion analysis in phenocrysts, suggests potential changes in the melt fragility and viscosity with dissolved H_2O content, thereby impacting the inversion temperature value. According to the chemical-based models discussed above, adding 3–5 wt% H_2O to the melt composition could decrease its viscosity by approximately 4 orders of magnitude. Moreover, our data were collected for a single-phase (liquid) melt, excluding the rheological effects of crystallization and CO_2 gas produced by carbonate thermal decomposition. While the presence of a crystals is expected to increase magma viscosity, the presence of a gas phase could produce either an increase or a decrease of magma viscosity depending on the deformation regime (Mader et al., 2013). Finally, the pressure-dependence of viscosity, although playing a secondary role at low pressure as those investigated here ($P = 100$ MPa; Russell et al., 2022), has been neglected. Precisely determining the comprehensive rheological behaviour of these magmas is essential for accurately modelling magma homogenization (mingling vs. mixing) and flow mobility (Colucci et al., 2024). Therefore, future research that focus on the rheology of multiphase, H_2O -bearing endoskarn melt from Vesuvius would be of great value.

5. Conclusions

Viscosity data for a phonotephrite from Vesuvius (Italy), contaminated by variable amounts of carbonate materials, show a viscosity crossover in the temperature space when CaO and CaO + MgO are added to the anhydrous starting material. The pristine melt shows the highest viscosity above a critical temperature of 750 °C, whereas it attains the lowest viscosity value below this threshold. The addition of CaO induces a viscosity variation significantly larger than that produced by CaO + MgO addition, pointing to a predominant role of CaO compared to MgO in affecting the viscosity of the silicate liquid. Viscosity estimates obtained by using empirical models from literature do not reproduce our experimental data set, particularly for high doped melts. Differently from chemically-based models, the Brillouin spectroscopy approach, combined with differential scanning calorimetry, provides the most accurate predictions for our viscosity data set. By interpolating Raman spectroscopy with viscometry data, we identified the formation of nanoheterogeneities during viscosity measurements and quantified their impact on melt viscosity.

This research establishes a foundation for understanding processes occurring within the volcano plumbing system, such as the interaction between magma and host carbonate rocks, the formation and homogenization of hybrid magma compositions (mingling versus mixing), and the flow behaviour of magmas at pre- and syn-eruptive conditions, where magmatic stoping can promote rapid host rock assimilation, CO_2 release, and enhanced eruption explosivity. These insights are especially relevant in volcanic contexts like Vesuvius where magma-carbonate interaction are well-documented. Further research is needed to comprehensively understand the additional rheological complexities of multiphase, H_2O -bearing contaminated melts.

CRedit authorship contribution statement

Gabriele Giuliani: Writing – original draft, Methodology, Formal analysis, Conceptualization. **Danilo Di Genova:** Writing – original draft, Methodology, Formal analysis, Conceptualization. **Fabrizio Di Fiore:** Writing – original draft, Methodology, Formal analysis, Conceptualization. **Pedro Valdivia:** Writing – original draft, Methodology, Formal analysis, Conceptualization. **Silvio Mollo:** Writing – original draft, Methodology, Formal analysis, Conceptualization. **Claudia Romano:** Writing – original draft, Methodology, Formal analysis, Conceptualization. **Tiziana Boffa Ballaran:** Writing – original draft, Methodology, Formal analysis, Conceptualization. **Alexander Kurnosov:** Writing – original draft, Methodology, Formal analysis, Conceptualization. **Alessandro Vona:** Writing – original draft, Methodology, Formal analysis, Conceptualization.

Declaration of competing interest

The authors declare that they have no known competing financial interests or personal relationships that could have appeared to influence the work reported in this paper.

Data availability

research data are available as supplementary material.

Acknowledgements

Two anonymous reviewers are thanked for their thoughtful comments that materially improved the presentation and discussions of our results. We are grateful to Don Porcelli for his helpful editorial guidance.

Appendix A. Supplementary data

Supplementary data to this article can be found online at <https://doi.org/10.1016/j.chemgeo.2024.122408>.

[org/10.1016/j.chemgeo.2024.122408](https://doi.org/10.1016/j.chemgeo.2024.122408).

References

- Al-Mukadam, R., Di Genova, D., Bornhöft, H., Deubener, J., 2020. High rate calorimetry derived viscosity of oxide melts prone to crystallization. *J. Non-Cryst. Solids* 536. <https://doi.org/10.1016/j.jnoncrysol.2020.119992>.
- Angell, C.A., 1995. *Relaxations in Complex Systems* (US Department of Commerce National Technical Information Service, ed. KL Ngai and GB Wright, 1985).
- Barberi, F., Leoni, L., 1980. Metamorphic carbonate ejecta from vesuvius plinian eruptions: evidence of the occurrence of shallow magma chambers (1). *Bull. Volc.* 43, 107–120.
- Bouhifd, M.A., Richet, P., Besson, P., Roskosz, M., Ingrin, J., 2004. Redox state, microstructure and viscosity of a partially crystallized basalt melt. *Earth Planet. Sci. Lett.* 218, 31–44. [https://doi.org/10.1016/S0012-821X\(03\)00641-1](https://doi.org/10.1016/S0012-821X(03)00641-1).
- Bruno, P.P.G., Cippitelli, G., Rapolla, A., 1998. Seismic study of the Mesozoic carbonate basement around Mt. Somma-Vesuvius, Italy. *J. Volcanol. Geotherm. Res.* 84, 311–322. [https://doi.org/10.1016/S0377-0273\(98\)00023-7](https://doi.org/10.1016/S0377-0273(98)00023-7).
- Buono, G., Pappalardo, L., Harris, C., Edwards, B.R., Petrosino, P., 2020. Magmatic stoping during the caldera-forming Pomici di Base eruption (Somma-Vesuvius, Italy) as a fuel of eruption explosivity. *Lithos* 370–371, 105628. <https://doi.org/10.1016/j.lithos.2020.105628>.
- Cassetta, M., Di Genova, D., Zanatta, M., Boffa Ballaran, T., Kurnosov, A., Giarola, M., Mariotto, G., 2021. Estimating the viscosity of volcanic melts from the vibrational properties of their parental glasses. *Sci. Rep.* 11 <https://doi.org/10.1038/s41598-021-92407-5>.
- Chadwick, J.P., Troll, V.R., Ginibre, C., Morgan, D., Gertisser, R., Waight, T.E., Davidson, J.P., 2007. Carbonate assimilation at merapi volcano, Java, Indonesia: insights from crystal isotope stratigraphy. *J. Petrol.* 48, 1793–1812. <https://doi.org/10.1093/petrology/egm038>.
- Chevrel, M.O., Giordano, D., Potuzak, M., Courtil, P., Dingwell, D.B., 2013. Physical properties of CaAl₂Si₂O₈-CaMgSi₂O₆-FeO-Fe₂O₃ melts: analogues for extra-terrestrial basalt. *Chem. Geol.* 346, 93–105. <https://doi.org/10.1016/j.chemgeo.2012.09.004>.
- Chiodini, G., Caliro, S., Aiuppa, A., Avino, R., Granieri, D., Moretti, R., Parello, F., 2011. First 13C/12C isotopic characterisation of volcanic plume CO₂. *Bull. Volcanol.* 73, 531–542. <https://doi.org/10.1007/s00445-010-0423-2>.
- Cioni, R., Marianelli, P., Santacroce, R., 1998. Thermal and compositional evolution of the shallow magma chambers of Vesuvius: evidence from pyroxene phenocrysts and melt inclusions. *J. Geophys. Res. Solid Earth* 103, 18277–18294. <https://doi.org/10.1029/98jb01124>.
- Colucci, S., Brogi, F., Sottili, G., Montagna, C.P., Papale, P., 2024. Short-term magma-carbonate interaction: a modelling perspective. *Earth Planet. Sci. Lett.* 628 <https://doi.org/10.1016/j.epsl.2024.118592>.
- Conte, A., Dolfi, D., Gaeta, M., Misiti, V., Mollo, S., Perinelli, C., Maria Dolfi, D., Gaeta, M., Misiti, V., Mollo, S., Perinelli, C., 2009. Experimental constraints on evolution of leucite-basanite magma at 1 and 10–4 GPa: implications for parental compositions of Roman high-potassium magmas. *Eur. J. Mineral.* 21, 763–782. <https://doi.org/10.1127/0935-1221/2009/0021-1934>.
- Dallai, L., Cioni, R., Boschi, C., D'Orlando, C., 2011. Carbonate-derived CO₂ purging magma at depth: influence on the eruptive activity of Somma-Vesuvius, Italy. *Earth Planet. Sci. Lett.* 310, 84–95. <https://doi.org/10.1016/j.epsl.2011.07.013>.
- Daly, R.A., 1910. *Origin of the Alkaline Rocks*.
- Davì, M., Behrens, H., Vetere, F., De Rosa, R., 2009. The viscosity of latitic melts from Lipari (Aeolian Islands, Italy): inference on mixing-mingling processes in magmas. *Chem. Geol.* 259, 89–97. <https://doi.org/10.1016/j.chemgeo.2008.10.009>.
- Deegan, F.M., Troll, V.R., Freda, C., Misiti, V., Chadwick, J.P., McLeod, C.L., Davidson, J.P., 2010. Magma-carbonate interaction processes and associated CO₂ release at Merapi volcano, Indonesia: insights from experimental petrology. *J. Petrol.* 51, 1027–1051. <https://doi.org/10.1093/petrology/egq010>.
- Del Moro, A., Fulignati, P., Marianelli, P., Sbrana, A., 2001. Magma contamination by direct wall rock interaction: constraints from xenoliths from the walls of a carbonate-hosted magma chamber (Vesuvius 1944 eruption). *J. Volcanol. Geotherm. Res.* 112, 15–24.
- Di Battistini, G., Montanini, A., Vernia, L., Bargossi, G.M., Castorina, F., 1998. Petrology and geochemistry of ultrapotassic rocks from the Montefiascone Volcanic Complex (Central Italy): magmatic evolution and petrogenesis. *Lithos* 43, 169–195.
- Di Battistini, G., Montanini, A., Vernia, L., Venturini, G., Tonarini, S., 2001. Petrology of melilite-bearing rocks from the Montefiascone Volcanic Complex (Roman Magmatic Province): new insights into the ultrapotassic volcanism of Central Italy. *Lithos* 59, 1–24. [https://doi.org/10.1016/S0012-4937\(01\)00054-8](https://doi.org/10.1016/S0012-4937(01)00054-8).
- Di Fiore, F., Vona, A., Kolzenburg, S., Mollo, S., Romano, C., 2021. An extended rheological map of pahoehoe—a'a transition. *J. Geophys. Res. Solid Earth* 126. <https://doi.org/10.1029/2021JB022035>.
- Di Fiore, F., Vona, A., Costa, A., Mollo, S., Romano, C., 2022. Quantifying the influence of cooling and shear rate on the disequilibrium rheology of a trachybasaltic melt from Mt. Etna. *Earth Planet. Sci. Lett.* 594, 117725 <https://doi.org/10.1016/j.epsl.2022.117725>.
- Di Fiore, F., Vona, A., Mollo, S., Nazzari, M., Giordano, G., Romano, C., 2023. Experimental insights on the shear-induced crystallization of a phonotephrite magma. *Chem. Geol.* 637 <https://doi.org/10.1016/j.chemgeo.2023.121682>.
- Di Fiore, F., Vona, A., Di Genova, D., Pontesilli, A., Calabrò, L., Mollo, S., Taddeucci, J., Romano, C., Scarlato, P., 2024. Magma titanium and iron contents dictate crystallization timescales and rheological behaviour in basaltic volcanic systems. *Commun. Earth Environ.* 5 <https://doi.org/10.1038/s43247-024-01452-1>.
- Di Genova, D., Hess, K.U., Chevrel, M.O., Dingwell, D.B., 2016. Models for the estimation of Fe³⁺/Fetot ratio in terrestrial and extraterrestrial alkali- and iron-rich silicate glasses using Raman spectroscopy. *Am. Mineral.* 101, 943–952. <https://doi.org/10.2138/am-2016-5534CCBYNCND>.
- Di Genova, D., Kolzenburg, S., Wiesmaier, S., Dallanave, E., Neuville, D.R., Hess, K.U., Dingwell, D.B., 2017a. A compositional tipping point governing the mobilization and eruption style of rhyolitic magma. *Nature* 552, 235–238. <https://doi.org/10.1038/nature24488>.
- Di Genova, D., Sicola, S., Romano, C., Vona, A., Fanara, S., Spina, L., 2017b. Effect of iron and nanolites on Raman spectra of volcanic glasses: a reassessment of existing strategies to estimate the water content. *Chem. Geol.* 475, 76–86. <https://doi.org/10.1016/j.chemgeo.2017.10.035>.
- Di Genova, D., Zandonà, A., Deubener, J., 2020. Unravelling the effect of nano-heterogeneity on the viscosity of silicate melts: Implications for glass manufacturing and volcanic eruptions. *J. Non-Cryst. Solids* 545. <https://doi.org/10.1016/j.jnoncrysol.2020.120248>.
- Di Genova, D., Bondar, D., Zandonà, A., Valdivia, P., Al-Mukadam, R., Fei, H., Withers, A.C., Boffa Ballaran, T., Kurnosov, A., McCammon, C., Deubener, J., Katsura, T., 2023. Viscosity of anhydrous and hydrous peridotite melts. *Chem. Geol.* 625 <https://doi.org/10.1016/j.chemgeo.2023.121440>.
- Di Muro, A., Métrich, N., Mercier, M., Giordano, D., Massare, D., Montagnac, G., 2009. Micro-Raman determination of iron redox state in dry natural glasses: application to peralkaline rhyolites and basalts. *Chem. Geol.* 259, 78–88. <https://doi.org/10.1016/j.chemgeo.2008.08.013>.
- Di Rocco, T., Freda, C., Gaeta, M., Mollo, S., Dallai, L., 2012. Magma chambers emplaced in carbonate substrate: petrogenesis of skarn and cumulate rocks and implications for CO₂ degassing in volcanic areas. *J. Petrol.* 53, 2307–2332. <https://doi.org/10.1093/petrology/egs051>.
- Di Stefano, F., Mollo, S., Scarlato, P., Nazzari, M., Bachmann, O., Caruso, M., 2018. Olivine compositional changes in primitive magmatic skarn environments: a reassessment of divalent cation partitioning models to quantify the effect of carbonate assimilation. *Lithos* 316–317, 104–121. <https://doi.org/10.1016/j.lithos.2018.07.008>.
- Dingwell, D.B., 1986. Viscosity-temperature relationships in the system Na₂Si₂O₅-Na₄Al₂O₅. *Geochim. Cosmochim. Acta* 50, 1261–1265. [https://doi.org/10.1016/0016-7037\(86\)90409-6](https://doi.org/10.1016/0016-7037(86)90409-6).
- Dingwell, D.B., Hess, K.U., Knoche, R., 1996. Granite and granitic pegmatite melts: volumes and viscosities. *Earth Environ. Sci. Trans. R. Soc. Edinburgh* 87, 65–72. <https://doi.org/10.1017/S026359330006489>.
- Douglas, R.W., Armstrong, W.L., Edward, J.P., Hall, D., 1965. A penetration viscometer. *Glass Technol.* 6, 52–55.
- Fernandez, A.N., Gasquet, D.R., 1994. Relative rheological evolution of chemically contrasted coeval magmas: example of the Tichka plutonic complex (Morocco). *Contrib. Mineral. Petrol.* 116, 316–326. <https://doi.org/10.1007/BF00306500>.
- Foland, K.A., Landoll, J.D., Henderson, C.M.B., Chen, J., 1993. Formation of co-genetic quartz and nepheline syenites. *Geochim. Cosmochim. Acta* 57, 697–704. [https://doi.org/10.1016/0016-7037\(93\)90380-F](https://doi.org/10.1016/0016-7037(93)90380-F).
- Freda, C., Gaeta, M., Misiti, V., Mollo, S., Dolfi, D., Scarlato, P., 2008. Magma-carbonate interaction: an experimental study on ultrapotassic rocks from Alban Hills (Central Italy). *Lithos* 101, 397–415. <https://doi.org/10.1016/j.lithos.2007.08.008>.
- Fulignati, P., Marianelli, P., 2007. Tracing volatile exsolution within the 472 AD “Pollena” magma chamber of Vesuvius (Italy) from melt inclusion investigation. *J. Volcanol. Geotherm. Res.* 161, 289–302. <https://doi.org/10.1016/j.jvolgeores.2006.12.011>.
- Fulignati, P., Marianelli, P., Santacroce, R., Sbrana, A., 2000. The skarn shell of the 1944 Vesuvius magma chamber. Genesis and P-T-X conditions from melt and fluid inclusion data. *Eur. J. Mineral.* 12, 1025–1039. <https://doi.org/10.1127/0935-1221/2000/0012-1025>.
- Fulignati, P., Marianelli, P., Santacroce, R., Sbrana, A., 2004. Probing the Vesuvius magma chamber-host rock interface through xenoliths. *Geol. Mag.* 141, 417–428. <https://doi.org/10.1017/S0016756804009392>.
- Gaeta, M., Di Rocco, T., Freda, C., 2009. Carbonate assimilation in open magmatic systems: the role of melt-bearing skarns and cumulate-forming processes. *J. Petrol.* 50, 361–385. <https://doi.org/10.1093/petrology/egp002>.
- Galeener, F.L., 1982. Planar rings in vitreous silica. *J. Non-Cryst. Solids* 49, 53–62.
- Gilg, H.A., Lima, A., Somma, R., Belkin, H.E., De Vivo, B., Ayuso, R.A., 2001. Isotope geochemistry and fluid inclusion study of skarns from Vesuvius. *Mineral. Petrol.* 73, 145–176.
- Giordano, D., Dingwell, D.B., 2003. Non-Arrhenian multicomponent melt viscosity: a model. *Earth Planet. Sci. Lett.* 208, 337–349. [https://doi.org/10.1016/S0012-821X\(03\)00042-6](https://doi.org/10.1016/S0012-821X(03)00042-6).
- Giordano, D., Russell, J.K., Dingwell, D.B., 2008. Viscosity of magmatic liquids: a model. *Earth Planet. Sci. Lett.* 271, 123–134. <https://doi.org/10.1016/j.epsl.2008.03.038>.
- Giordano, D., Ardia, P., Romano, C., Dingwell, D.B., Di Muro, A., Schmidt, M.W., Mangiacapra, A., Hess, K.U., 2009. The rheological evolution of alkaline Vesuvius magmas and comparison with alkaline series from the Phlegrean Fields, Etna Stromboli and Teide. *Geochim. Cosmochim. Acta* 73, 6613–6630. <https://doi.org/10.1016/j.gca.2009.07.033>.
- Goff, F., Love, S.P., Warren, R.G., Counce, D., Obenholzer, J., Siebe, C., Schmidt, S.C., 2001. Passive infrared remote sensing evidence for large, intermittent CO₂ emissions at Popocatepetl volcano, Mexico. *Chem. Geol.* 177, 133–156. [https://doi.org/10.1016/S0009-2541\(00\)00387-9](https://doi.org/10.1016/S0009-2541(00)00387-9).
- Gottsmann, J., Giordano, D., Dingwell, D.B., 2002. Predicting shear viscosity during volcanic processes at the glass transition: a calorimetric calibration. *Earth Planet. Sci. Lett.* 198, 417–427. [https://doi.org/10.1016/S0012-821X\(02\)00522-8](https://doi.org/10.1016/S0012-821X(02)00522-8).

- Gozzi, F., Gaeta, M., Freda, C., Mollo, S., Di Rocco, T., Marra, F., Dallai, L., Pack, A., 2014. Primary magmatic calcite reveals origin from crustal carbonate. *Lithos* 190–191, 191–203. <https://doi.org/10.1016/j.lithos.2013.12.008>.
- Hildreth, W., Moorbath, S., 1988. Crustal contributions to arc magmatism in the Andes of Central Chile. *Contrib. Mineral. Petrol.* 98, 455–489. <https://doi.org/10.1007/BF00372365>.
- Huppert, H.E., Stephen, R., Sparks, R.S.J., Turner, J.S., 1984. Some effects of viscosity on the dynamics of replenished magma chambers. *J. Geophys. Res. Solid Earth* 89, 6857–6877. <https://doi.org/10.1029/JB089iB08p06857>.
- Hushur, A., Manghni, M.H., Williams, Q., Dingwell, D.B., 2013. A high-temperature Brillouin scattering study on four compositions of haplogranitic glasses and melts: high-frequency elastic behavior through the glass transition. *Am. Mineral.* 98, 367–375. <https://doi.org/10.2138/am.2013.4198>.
- Iacono Marziano, G., Gaillard, F., Pichavant, M., 2007a. Limestone assimilation and the origin of CO₂ emissions at the Alban Hills (Central Italy): constraints from experimental petrology. *J. Volcanol. Geotherm. Res.* 166, 91–105. <https://doi.org/10.1016/j.jvolgeores.2007.07.001>.
- Iacono Marziano, G., Schmidt, B.C., Dolfi, D., 2007b. Equilibrium and disequilibrium degassing of a phonolitic melt (Vesuvius AD 79 “white pumice”) simulated by decompression experiments. *J. Volcanol. Geotherm. Res.* 161, 151–164. <https://doi.org/10.1016/j.jvolgeores.2006.12.001>.
- Iacono Marziano, G., Gaillard, F., Pichavant, M., 2008. Limestone assimilation by basaltic magmas: an experimental re-assessment and application to Italian volcanoes. *Contrib. Mineral. Petrol.* 155, 719–738. <https://doi.org/10.1007/s00410-007-0267-8>.
- Jolis, E.M., Freda, C., Troll, V.R., Deegan, F.M., Blythe, L.S., McLeod, C.L., Davidson, J.P., 2013. Experimental simulation of magma-carbonate interaction beneath Mt. Vesuvius, Italy. *Contrib. Mineral. Petrol.* 166, 1335–1353. <https://doi.org/10.1007/s00410-013-0931-0>.
- Jolis, E.M., Troll, V.R., Harris, C., Freda, C., Gaeta, M., Orsi, G., Siebe, C., 2015. Skarn xenolith record crustal CO₂ liberation during Pompeii and Pollena eruptions, Vesuvius volcanic system, Central Italy. *Chem. Geol.* 415, 17–36. <https://doi.org/10.1016/j.chemgeo.2015.09.003>.
- Kerrick, D.M., 1977. The genesis of zoned skarns in the Sierra Nevada, California. *J. Petrol.* 18, 144–181. <https://doi.org/10.1093/petrology/18.1.144>.
- Kleest, C., Webb, S.L., 2021. Influence of CO₂ on the rheology of melts from the Colli Albani Volcanic District (Italy): foidite to phonolite. *Contrib. Mineral. Petrol.* 176, 1–15. <https://doi.org/10.1007/s00410-021-01838-w>.
- Kleest, C., Webb, S.L., 2022. Influence of Fe²⁺/Fetot on the viscosity of melts from the Colli Albani Volcanic District (Italy) – foidite to phonolite. *J. Volcanol. Geotherm. Res.* 431. <https://doi.org/10.1016/j.jvolgeores.2022.107649>.
- Kleest, C., Webb, S.L., Fanara, S., 2020. Rheology of melts from the colli albani volcanic district (Italy): a case study. *Contrib. Mineral. Petrol.* 175. <https://doi.org/10.1007/s00410-020-01720-1>.
- Knuever, M., Mele, D., Sulpizio, R., 2023a. Mineralization and skarn formation associated with alkaline magma chambers emplaced in a limestone basement: a review. *Minerals*. <https://doi.org/10.3390/min1309184>.
- Knuever, M., Sulpizio, R., Mele, D., Costa, A., 2023b. Magma–rock interactions: a review of their influence on magma rising processes with emphasis on short-timescale assimilation of carbonate rocks. *Geol. Soc. London Spec. Publ.* 520, 101–120. <https://doi.org/10.1144/sp520-2021-177>.
- Knuever, M., Sulpizio, R., Mele, D., Pisello, A., Costa, A., Perugini, D., Vetere, F., 2023c. Decarbonation and clast dissolution timescales for short-term magma-carbonate interactions in the volcanic feeding system and their influence on eruptive dynamics: insights from experiments at atmospheric pressure. *Chem. Geol.* 639. <https://doi.org/10.1016/j.chemgeo.2023.121724>.
- Langhammer, D., Di Genova, D., Steinle-Neumann, G., 2021. Modeling the viscosity of anhydrous and hydrous volcanic melts. *Geochem. Geophys. Geosyst.* 22. <https://doi.org/10.1029/2021GC009918>.
- Langhammer, D., Di Genova, D., Steinle-Neumann, G., 2022. Modeling viscosity of volcanic melts with artificial neural networks. *Geochem. Geophys. Geosyst.* 23. <https://doi.org/10.1029/2022GC010673>.
- Le Losq, C., Neuville, D.R., 2013. Effect of the Na/K mixing on the structure and the rheology of tectosilicate silica-rich melts. *Chem. Geol.* 346, 57–71. <https://doi.org/10.1016/j.chemgeo.2012.09.009>.
- Lentz, D.R., 1999. Carbonatite genesis: a reexamination of the role of intrusion-related pneumatolytic skarn processes in limestone melting. *Geology* 27, 335–338. [https://doi.org/10.1130/0091-7613\(1999\)027<0335:CGAROT>2.3.CO;2](https://doi.org/10.1130/0091-7613(1999)027<0335:CGAROT>2.3.CO;2).
- Liebske, C., Behrens, H., Holtz, F., Lange, R.A., 2003. The influence of pressure and composition on the viscosity of andesitic melts. *Geochim. Cosmochim. Acta* 67, 473–485. [https://doi.org/10.1016/S0016-7037\(02\)01139-0](https://doi.org/10.1016/S0016-7037(02)01139-0).
- Lustrino, M., Luciani, N., Stagno, V., Narzisi, S., Masotta, M., Scarlato, P., 2022. Experimental evidence on the origin of Ca-rich carbonated melts formed by interaction between sedimentary limestones and mantle-derived ultrabasic magmas. *Geology* 50, 476–480. <https://doi.org/10.1130/G49621.1>.
- Macdonald, R., Bagiński, B., Rolandi, G., De Vivo, B., Koczyńska, A., 2016. Petrology of parasitic and eccentric cones on the flanks and base of Somma-Vesuvius. *Mineral. Petrol.* 110, 65–85. <https://doi.org/10.1007/s00710-015-0410-6>.
- Mader, H.M., Llewellyn, E.W., Mueller, S.P., 2013. The rheology of two-phase magmas: a review and analysis. *J. Volcanol. Geotherm. Res.* <https://doi.org/10.1016/j.jvolgeores.2013.02.014>.
- Mauro, J.C., Yue, Y., Ellison, A.J., Gupta, P.K., Allan, D.C., 2009. Viscosity of glass-forming liquids. *Proc. Natl. Acad. Sci.* 106, 19780–19784. <https://doi.org/10.1073/pnas.0911705106>.
- Mazurin, O.V., 1977. Relaxation phenomena in glass. *J. Non-Cryst. Solids* 25, 129–169. [https://doi.org/10.1016/0022-3093\(77\)90092-8](https://doi.org/10.1016/0022-3093(77)90092-8).
- Meerlender, G., 1974. Viskositäts-temperatur-verhalten des standardglases I der DGG. *Glas. Berichte* 1, 1–3.
- Michaud, V., 1995. Crustal xenoliths in recent hawaiites from Mount Etna, Italy: evidence for alkali exchanges during magma-wall rock interaction. *Chem. Geol.* 122, 21–42. [https://doi.org/10.1016/0009-2541\(94\)00133-S](https://doi.org/10.1016/0009-2541(94)00133-S).
- Mollo, S., Vona, A., 2014. The geochemical evolution of clinopyroxene in the Roman Province: a window on decarbonation from wall-rocks to magma. *Lithos* 192–195, 1–7. <https://doi.org/10.1016/j.lithos.2014.01.009>.
- Mollo, S., Vinciguerra, S., Iezzi, G., Iarocci, A., Scarlato, P., Heap, M.J., Dingwell, D.B., 2011. Volcanic edifice weakening via devolatilization reactions. *Geophys. J. Int.* 186, 1073–1077. <https://doi.org/10.1111/j.1365-246X.2011.05097.x>.
- Mollo, S., Heap, M.J., Iezzi, G., Hess, K.U., Scarlato, P., Dingwell, D.B., 2012. Volcanic edifice weakening via decarbonation: a self-limiting process? *Geophys. Res. Lett.* 39, 1–6. <https://doi.org/10.1029/2012GL052613>.
- Morgavi, D., Laumonier, M., Petrelli, M., Dingwell, D.B., 2022. Decrypting magma mixing in igneous systems. *Rev. Mineral. Geochem.* 87, 607–638. <https://doi.org/10.2138/rmg.2022.87.13>.
- Morris, R.A., Canil, D., 2024. Crust-derived CO₂ production from a shallow pluton in limestone is driven by metamorphic decarbonation, not assimilation. *Geochem. Geophys. Geosyst.* 25, 1–18. <https://doi.org/10.1029/2024GC0011485>.
- Moynihan, C.T., Easteal, A.J., De Bolt, M.A.N.N., Tucker, J., 1976. Dependence of the fictive temperature of glass on cooling rate. *J. Am. Ceram. Soc.* 59, 12–16. <https://doi.org/10.1111/j.1151-2916.1976.tb09376.x>.
- Mysen, B., Virgo, D., Seifert, F.A., 1985. Relationships between properties and structure of aluminosilicate melts. *Am. Mineral.* 70, 88–105.
- Okumura, S., Uesugi, K., Goto, A., Sakamaki, T., Matsumoto, K., Takeuchi, A., Miyake, A., 2022. Rheology of nanocrystal-bearing andesite magma and its roles in explosive volcanism. *Commun. Earth Environ.* 3, 1–7. <https://doi.org/10.1038/s43247-022-00573-9>.
- Pasquarello, A., Car, R., 1998. Identification of Raman defect lines as signatures of ring structures in vitreous silica. *Phys. Rev. Lett.* 80, 5145–5147. <https://doi.org/10.1103/PhysRevLett.80.5145>.
- Plazek, D.J., Ngai, K.L., 1991. Correlation of polymer segmental chain dynamics with temperature-dependent time-scale shifts. *Macromolecules* 24, 1222–1224.
- Potuzak, M., Nichols, A.R.L., Dingwell, D.B., Clague, D.A., 2008. Hyperquenched volcanic glass from Loihi Seamount, Hawaii. *Earth Planet. Sci. Lett.* 270, 54–62. <https://doi.org/10.1016/j.epsl.2008.03.018>.
- Rahmani, A., Benoit, M., Benoit, C., 2003. Signature of small rings in the Raman spectra of normal and compressed amorphous silica: a combined classical and ab initio study. *Phys. Rev. B* 68, 1–21. <https://doi.org/10.1103/PhysRevB.68.184202>.
- Richet, P., Nidaira, A., Neuville, D.R., Atake, T., 2009. Aluminum speciation, vibrational entropy and short-range order in calcium aluminosilicate glasses. *Geochim. Cosmochim. Acta* 73, 3894–3904. <https://doi.org/10.1016/j.gca.2009.03.041>.
- Richet, P., Polian, A., 1998. Water as a dense icelike component in silicate glasses. *Science* 281, 396–398.
- Richet, P., Lejeune, A.M., Holtz, F., Roux, J., 1996. Water and the viscosity of andesite melts. *Chem. Geol.* 128, 185–197.
- Rogers, N.W., Hawkesworth, C.J., Parker, R.J., Marsh, J.S., 1985. The geochemistry of potassic lavas from Vulcini, Central Italy, and implications for mantle enrichment processes beneath the Roman region. *Contrib. Mineral. Petrol.* 90, 244–257.
- Rosi, M., Santacroce, R., 1983. The AD 472 “Pollena” eruption: volcanological and petrological data for this poorly-known, Pliniintype event at Vesuvius. *Journal of Volcanology and Geothermal Research* 17, 249–271.
- Russell, J.K., Hess, K.U., Dingwell, D.B., 2022. Models for viscosity of geological melts. *Rev. Mineral. Geochem.* 87, 841–885. <https://doi.org/10.2138/rmg.2022.87.18>.
- Santacroce, R., Cioni, R., Marianelli, P., Sbrana, A., Sulpizio, R., Zanchetta, G., Donahue, D.J., Joron, J.L., 2008. Age and whole rock-glass compositions of proximal pyroclastics from the major explosive eruptions of Somma-Vesuvius: a review as a tool for distal tephrostratigraphy. *J. Volcanol. Geotherm. Res.* 177, 1–18. <https://doi.org/10.1016/j.jvolgeores.2008.06.009>.
- Scaillet, B., Pichavant, M., Cioni, R., 2008. Upward migration of Vesuvius magma chamber over the past 20,000 years. *Nature* 455, 216–219. <https://doi.org/10.1038/nature07232>.
- Scarani, A., Vona, A., Di Genova, D., Al-Mukadam, R., Romano, C., Deubener, J., 2022a. Determination of cooling rates of glasses over four orders of magnitude. *Contrib. Mineral. Petrol.* 177. <https://doi.org/10.1007/s00410-022-01899-5>.
- Scarani, A., Zandonà, A., Di Fiore, F., Valdivia, P., Putra, R., Miyajima, N., Bornhöft, H., Vona, A., Deubener, J., Romano, C., Di Genova, D., 2022b. A chemical threshold controls nanocrystallization and degassing behaviour in basaltic magmas. *Commun. Earth Environ.* 3, 284. <https://doi.org/10.1038/s43247-022-00615-2>.
- Scarani, A., Faranda, C.F., Vona, A., Speranza, F., Giordano, G., Rotolo, S.G., Romano, C., 2023. Timescale of emplacement and rheomorphism of the green tuff ignimbrite (Pantelleria, Italy). *J. Geophys. Res. Solid Earth* 128. <https://doi.org/10.1029/2022JB026257>.
- Schaaf, P., Stimac, J.I.M., Siebe, C., Macías, J.L., 2005. Geochemical evidence for mantle origin and crustal processes in volcanic rocks from Popocatepetl and surrounding monogenetic volcanoes, Central Mexico. *J. Petrol.* 46, 1243–1282.
- Scherer, G.W., 1984. Use of the adam-gibbs equation in the analysis of structural relaxation. *J. Am. Ceram. Soc.* 67, 504–511. <https://doi.org/10.1111/j.1151-2916.1984.tb19643.x>.
- Schiavi, F., Bolfan-Casanova, N., Withers, A.C., Médard, E., Laumonier, M., Laporte, D., Flaherty, T., Gómez-Ulla, A., 2018. Water quantification in silicate glasses by Raman spectroscopy: correcting for the effects of focality, density and ferric iron. *Chem. Geol.* 483, 312–331. <https://doi.org/10.1016/j.chemgeo.2018.02.036>.
- Sharma, S.K., Mammone, J.F., Nicol, M.F., 1981. Raman investigation of ring configurations in vitreous silica. *Nature*. <https://doi.org/10.1038/292140a0>.

- Sinogeikin, S., Bas, M., Prakapenka, V., Lakshtanov, D., Shen, G., Sanchez-Valle, C., Rivers, M., 2006. Brillouin spectrometer interfaced with synchrotron radiation for simultaneous x-ray density and acoustic velocity measurements. *Rev. Sci. Instrum.* 77, 103905 <https://doi.org/10.1063/1.2360884>.
- Sklyarov, E.V., Lavrenchuk, A.V., Doroshkevich, A.G., Starikova, A.E., Kanakin, S.V., 2021. Pyroxenite as a product of mafic-carbonate melt interaction (Tazheran massif, west baikal area, Russia). *Minerals* 11. <https://doi.org/10.3390/min11060654>.
- Sparks, R.S.J., Marshall, L.A., 1986. Thermal and mechanical constraints on mixing between mafic and silicic magmas. *J. Volcanol. Geotherm. Res.* 29, 99–124. [https://doi.org/10.1016/0377-0273\(86\)90041-7](https://doi.org/10.1016/0377-0273(86)90041-7).
- Stabile, P., Carroll, M.R., 2019. Petrologic experimental data on vesuvius and campi flegrei magmatism: a review. In: *Vesuvius, Campi Flegrei, and Campanian Volcanism*. Elsevier, pp. 323–369. <https://doi.org/10.1016/B978-0-12-816454-9.00013-4>.
- Stabile, P., Sicola, S., Giuli, G., Paris, E., Carroll, M.R., Deubener, J., Di Genova, D., 2021. The effect of iron and alkali on the nanocrystal-free viscosity of volcanic melts: a combined Raman spectroscopy and DSC study. *Chem. Geol.* 559 <https://doi.org/10.1016/j.chemgeo.2020.119991>.
- Stevenson, R.J., Dingwell, D.B., Webb, S.L., Bagdassarov, N.S., 1995. The equivalence of enthalpy and shear stress relaxation in rhyolitic obsidians and quantification of the liquid-glass transition in volcanic processes. *J. Volcanol. Geotherm. Res.* 68, 297–306. [https://doi.org/10.1016/0377-0273\(95\)00015-1](https://doi.org/10.1016/0377-0273(95)00015-1).
- Sulpizio, R., Mele, D., Dellino, P., La Volpe, L., 2005. A complex, Subplinian-type eruption from low-viscosity, phonolitic to tephri-phonolitic magma: the AD 472 (Pollena) eruption of Somma-Vesuvius, Italy. *Bull. Volcanol.* 67, 743–767. <https://doi.org/10.1007/s00445-005-0414-x>.
- Sulpizio, R., Mele, D., Dellino, P., La Volpe, L., 2007. Deposits and physical properties of pyroclastic density currents during complex Subplinian eruptions: the AD 472 (Pollena) eruption of Somma-Vesuvius, Italy. *Sedimentology* 54, 607–635. <https://doi.org/10.1111/j.1365-3091.2006.00852.x>.
- Troll, V.R., Hilton, D.R., Jolis, E.M., Chadwick, J.P., Blythe, L.S., Deegan, F.M., Schwarzkopf, L.M., Zimmer, M., 2012. Crustal CO₂ liberation during the 2006 eruption and earthquake events at Merapi volcano, Indonesia. *Geophys. Res. Lett.* 39 <https://doi.org/10.1029/2012GL051307>.
- Valdivia, P., Zandonà, A., Kurnosov, A., Ballaran, T.B., Deubener, J., Di Genova, D., 2023. Are volcanic melts less viscous than we thought? The case of Stromboli basalt. *Contrib. Mineral. Petrol.* 178 <https://doi.org/10.1007/s00410-023-02024-w>.
- Valdivia, P., Zandonà, A., Löschmann, J., Bondar, D., Genevois, C., Allix, M., Miyajima, N., Kurnosov, A., Boffa Ballaran, T., Di Fiore, F., Vona, A., Romano, C., Deubener, J., Bamber, E.C., Di Genova, D., 2024. Nanoscale chemical heterogeneities control magma viscosity and failure. *Under Rev.* 1–25 <https://doi.org/10.21203/rs.3.rs-3891365/v1>.
- Verdurme, P., Le Losq, C., Chevrel, M.O., Pannefieu, S., Médard, E., Berthod, C., Komorowski, J.C., Bachelery, P., Neuville, D.R., Gurioli, L., 2023. Viscosity of crystal-free silicate melts from the active submarine volcanic chain of Mayotte. *Chem. Geol.* 620 <https://doi.org/10.1016/j.chemgeo.2023.121326>.
- Villemant, B., Michaud, V., Metrich, N., 1993. Wall rock-magma interactions in Etna, Italy, studied by U-Th disequilibrium and rare earth element systematics. *Geochim. Cosmochim. Acta* 57, 1169–1180. [https://doi.org/10.1016/0016-7037\(93\)90055-2](https://doi.org/10.1016/0016-7037(93)90055-2).
- Vona, A., Romano, C., Giordano, G., Sulpizio, R., 2020. Linking magma texture, rheology and eruptive style during the 472 AD Pollena Subplinian eruption (Somma-Vesuvius). *Lithos* 370–371. <https://doi.org/10.1016/j.lithos.2020.105658>.
- Wang, Z., Cooney, T.F., Sharma, S.K., 1993. High temperature structural investigation of Na₂O-0.5Fe₂O₃-3SiO₂ and Na₂O-FeO-3SiO₂ melts and glasses. *Contr. Mineral. and Petrol.* 115, 112–122. <https://doi.org/10.1007/BF00712983>.
- Wang, Z., Cooney, T.F., Sharma, S.K., 1995. In situ structural investigation of iron-containing silicate liquids and glasses. *Geochim. Cosmochim. Acta* 59, 1571–1577.
- Webb, S.L., Dingwell, D.B., 1990. Non-Newtonian rheology of igneous melts at high stresses and strain rates: experimental results for rhyolite, andesite, basalt, and nephelinite. *J. Geophys. Res.* 95 <https://doi.org/10.1029/jb095i01p15695>.
- Wenzel, T., Baumgartner, L.P., Brugmann, G.E., Konnikov, E.G., Kislov, E.V., 2002. Partial melting and assimilation of dolomitic xenoliths by mafic magma: the iokodovyren intrusion (North Baikal Region, Russia). *J. Petrol.* 43, 2049–2074. <https://doi.org/10.1093/petrology/43.11.2049>.
- Whitley, S., Halama, R., Gertisser, R., Preece, K., Deegan, F.M., Troll, V.R., 2020. Magmatic and metasomatic effects of magma-carbonate interaction recorded in calc-silicate xenoliths from Merapi volcano (Indonesia). *J. Petrol.* 61 <https://doi.org/10.1093/petrology/egaa048>.
- Whitney, D.L., Evans, B.W., 2010. Abbreviations for names of rock-forming minerals. *Am. Mineral.* 95, 185–187. <https://doi.org/10.2138/am.2010.3371>.
- Whittington, A.G., Richet, P., Linard, Y., Holtz, F., 2001. The viscosity of hydrous phonolites and trachytes. *Chem. Geol.* 174, 209–223.
- Whittington, A.G., Richet, P., Polian, A., 2012. Amorphous materials: properties, structure, and durability: water and the compressibility of silicate glasses: a Brillouin spectroscopic study. *Am. Mineral.* 97, 455–467.
- Wilding, M.C., Webb, S.L., Dingwell, D.B., 1995. Evaluation of a relaxation geospeedometer for volcanic glasses. *Chem. Geol.* 125, 137–148. [https://doi.org/10.1016/0009-2541\(95\)00067-V](https://doi.org/10.1016/0009-2541(95)00067-V).
- Woods, A.W., Cowan, A., 2009. Magma mixing triggered during volcanic eruptions. *Earth Planet. Sci. Lett.* 288, 132–137. <https://doi.org/10.1016/j.epsl.2009.09.015>.
- Yue, Y., Von der Ohe, R., Jensen, S.L., 2004. Fictive temperature, cooling rate, and viscosity of glasses. *J. Chem. Phys.* 120, 8053–8059. <https://doi.org/10.1063/1.1689951>.
- Zandonà, A., Scarani, A., Löschmann, J., Cicconi, M.R., Di Fiore, F., de Ligny, D., Deubener, J., Vona, A., Allix, M., Di Genova, D., 2023. Non-stoichiometric crystal nucleation in a spodumene glass containing TiO₂ as seed former: effects on the viscosity of the residual melt. *J. Non-Cryst. Solids* 619, 122563. <https://doi.org/10.1016/j.jnoncrysol.2023.122563>.
- Zheng, Q., Mauro, J.C., Ellison, A.J., Potuzak, M., Yue, Y., 2011. Universality of the high-temperature viscosity limit of silicate liquids. *Phys. Rev. B* 83, 212202. <https://doi.org/10.1103/PhysRevB.83.212202>.